

Review

# Review on the Solid-State Welding of Steels: Diffusion Bonding and Friction Stir Welding Processes

Mahmoud Khedr<sup>1,2,\*</sup> , Atef Hamada<sup>2,\*</sup> , Antti Järvenpää<sup>2</sup> , Sally Elkatatny<sup>3</sup>  and Walaa Abd-Elaziem<sup>4,\*</sup>

<sup>1</sup> Mechanical Engineering Department, Faculty of Engineering at Shoubra, Benha University, Cairo 11629, Egypt

<sup>2</sup> Kerttu Saalasti Institute, Future Manufacturing Technologies (FMT), University of Oulu, Pajatie 5, FI-85500 Nivala, Finland

<sup>3</sup> Mechanical Engineering Department, Faculty of Engineering, Suez Canal University, Ismailia 41522, Egypt

<sup>4</sup> Department of Mechanical Design and Production Engineering, Faculty of Engineering, Zagazig University, Zagazig 44519, Egypt

\* Correspondence: mahmoud.khedr.mk@gmail.com or mahmoud.khedr@feng.bu.edu.eg (M.K.); atef.hamadasaleh@oulu.fi (A.H.); walaa.abdelal@ejust.edu.eg (W.A.-E.); Tel.: +2-01025512986 (M.K.); +358-452516553 (A.H.)

**Abstract:** Solid-state welding (SSW) is a relatively new technique, and ongoing research is being performed to fulfill new design demands, deal with contemporary material advancements, and overcome welding defects associated with traditional welding techniques. This work provides an in-depth examination of the advancements in the solid-state welding of steels through diffusion bonding (DB) and friction stir welding (FSW). Considerable attention was given to DB of steel, which overcame the difficulties of segregation, cracking, and distortion stresses that are usually formed in liquid-phase welding techniques. The defects that affected DB included two types: two-dimensional defects of a metallic lattice, i.e., phases and grain boundaries, and three-dimensional defects, i.e., precipitation. FSW, on the other hand, was distinguishable by the use of relatively low heat input when compared to fusion welding processes such as tungsten inert gas (TIG), resulting in the formation of a limited heat-affected zone. Moreover, fine grain structures were formed in the FSW interface because of the stirring tool's severe plastic deformation, which positively affected the strength, ductility, and toughness of the FSW joints. For instance, higher strength and ductility were reported in joints produced by FSW than in those produced by TIG. Nevertheless, the HAZ width of the specimens welded by FSW was approximately half the value of the HAZ width of the specimens welded by TIG. Some defects associated with FSW related to the diffusion of elements, such as C/Cr atoms, through the weld zone, which affected the local chemical composition due to the formation of rich/depleted regions of the diffused atoms. Moreover, the lack-of-fill defect may exist when inappropriate welding conditions are implemented. On the other hand, the stirring tool was subjected to extensive wear because of the high hardness values, which negatively affected the economical usage of the FSW process. A summary of the results is presented, along with recommendations for future studies aimed at addressing existing difficulties and advancing the solid-state technology for steel.

**Keywords:** solid-state welding; diffusion bonding; friction stir processing; steel; microstructures



**Citation:** Khedr, M.; Hamada, A.; Järvenpää, A.; Elkatatny, S.; Abd-Elaziem, W. Review on the Solid-State Welding of Steels: Diffusion Bonding and Friction Stir Welding Processes. *Metals* **2023**, *13*, 54. <https://doi.org/10.3390/met13010054>

Academic Editor: Yongxian Huang

Received: 23 November 2022

Revised: 15 December 2022

Accepted: 21 December 2022

Published: 25 December 2022



**Copyright:** © 2022 by the authors. Licensee MDPI, Basel, Switzerland. This article is an open access article distributed under the terms and conditions of the Creative Commons Attribution (CC BY) license (<https://creativecommons.org/licenses/by/4.0/>).

## 1. Introduction

Welding is a joining process that permanently connects solid parts and forms components that cannot be divided without causing damage. Furthermore, welding is the most efficient and economical way to join similar or dissimilar materials with or without using filler material, heat, or external pressure. Welding can be processed in a variety of environments, including outdoors, inside, underwater, and even in outer space [1,2]. The two main categories of welding methods, solid-state welding (SSW) and fusion welding, are processes to join metals. Fusion welding can be defined as the melting process of parent

materials on facing surfaces with a filler material to form a weld bead. The fusion welding process comprises gas welding, arc welding, and intense-energy beam welding [3,4]. Such welding processes have many applications in different industrial sections, such as the manufacture of automobile bodies, aircraft frames, boilers, pressure vessels, ships, and tanks, as well as structural work and the repair of defects in both welded and cast products. However, welding has several drawbacks, such as developing internal stresses within the weld components, distortions, microstructure changes in the welded region, and harmful effects such as flashlights, ultra-violet radiation, high temperatures, and fumes [5,6]. Moreover, there are several concerns to be considered when welding dissimilar joints using the traditional fusion welding processes, including the selection of filler metals, differences in melting points, mechanical properties, and thermal expansion of the base metals [7,8]. Additionally, the formation of intermetallic compounds (IC) can produce brittle metal joints that have mutual solubility limitations, i.e., welding Al/stainless steel, Al/carbon steel, Al/Cu, Cu/Ti alloys, Al/Mg alloys, and W-Cu/Cu alloys [9,10]. Researchers have thoroughly investigated the metals joined by the various fusion welding techniques used to create assemblies made up of multi-component structures. However, these techniques require high-cost machines. Moreover, the fume and gas emissions during fusion welding cause air pollution in the workplace and, consequently, the health effects on humans and the environment are significant [11–13].

The advancement of technology in the fields of missiles and rockets, atomic energy, and electronics has increased and created new challenges for metal joining engineers, particularly in areas involving dissimilar metal junctions. Traditional bonding techniques are frequently difficult to apply or produce unsatisfactory bonds for specific applications [10,14]. The growing demand for increased productivity, efficiency, welding quality, and safety poses challenges to traditional fusion welding processes [15,16]. These welding processes are unable to deal with these challenges as materials become more sophisticated and complicated to achieve more specific properties [17,18].

On the other hand, SSW is a new technique designed to fulfill new design demands, deal with contemporary material advancements [19,20], and overcome welding defects and problems associated with traditional welding processes [21,22].

In SSW processes, no heat is applied directly. Instead, in most cases, sufficient pressure is applied. Thus, the heat is generated at the contact zone; however, this temperature usually remains below the melting point of the base components [23,24]. As there is no melting in SSW, the possibility of forming IC is reduced. Based on the previous reasons, SSW processes can successfully join dissimilar metals with little difficulty. However, these processes do not always provide the desired joint characteristics for special applications [25,26]. Figure 1 shows the main techniques of solid-state welding (SSW), such as diffusion bonding (DB), friction stir welding (FSW), forge welding (FW), cold welding (CW), and explosion welding (EW). This paper comprehensively reviews the research status and advancements in DB and FSW of steel joints. This paper provides a detailed discussion of the evolution of steel microstructures using solid-state welding techniques.

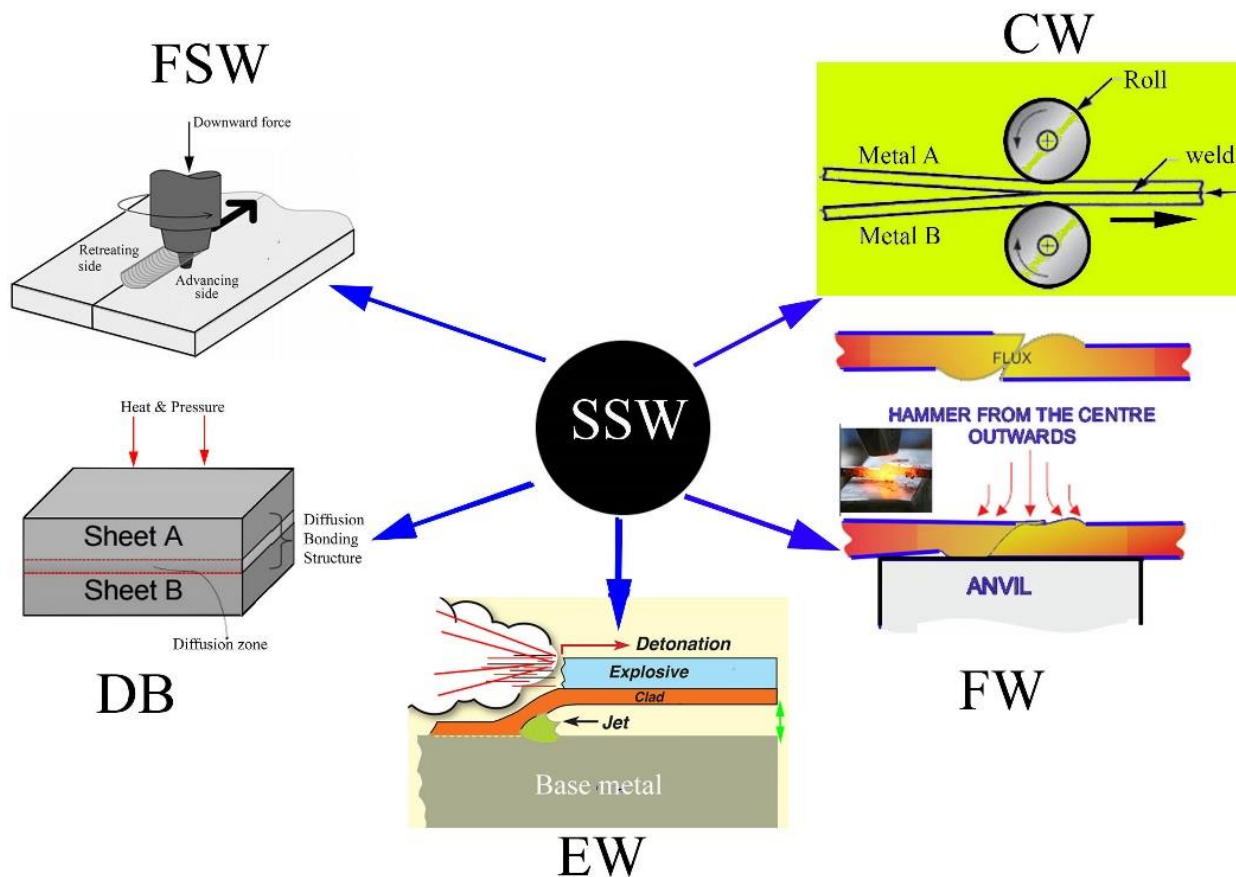


Figure 1. Most common techniques of solid-state welding (SSW).

## 2. Solid-State Welding (SSW)

SSW can be defined as welding processes in which welding is performed through coalescence at a lesser temperature than the base material's melting temperature and without using filler metal. In some SSW processes, pressure can be used. The advantages of SSW joints can be summarized as follows: SSW techniques are typically free of several solidification defects, such as hot cracking, gas porosity, and nonmetallic inclusions, which may be present throughout fusion-welding processes [19,27,28]. The welded materials' bonding is due to their interface atoms [29]. Thus, processes of SSW may alternatively be referred to as "solid-state bonding" [19]. Additionally, the welded zone's mechanical properties are nearly identical to or very close to those of the base metals. Solid-state welding techniques can easily weld dissimilar joints such as Al/Steel alloys, Al/Cu alloys, Cu/Ti alloys, Al/Mg alloys, and W-Cu/Cu alloys, among others [21,30–32]. However, SSW has some limitations. To improve the contact between the two base metals, SSW usually requires careful surface preparation before welding, such as oxide removal, degreasing, brushing, and/or sandblasting [23,24,33]. Additionally, most SSW equipment is expensive compared to ordinary fusion welding techniques.

### 2.1. Diffusion Bonding (DB)

DB is a solid-state joining technique that can be achieved with no need for a liquid interface, brazing, or cast product creation through melting and solidification [34]. DB can produce a solid-state bond between similar and different materials under a certain load at temperatures less than the melting temperature of the welded materials. An inert atmosphere or vacuum (a nonoxidizing environment) is required to protect the faying surface from oxidation. DB is based on the solid-state diffusion principle, in which the atoms of the solid materials intersperse themselves over time at high temperatures and pressure to form a high-quality bond between the base materials. DB can eliminate

defects, segregation problems, distortion stresses, and cracking that are usually formed in liquid-phase welding techniques [35]. However, DB is generally associated with a certain deformation at the interface of the joined components [36,37]. This deformation mainly depends on three crucial parameters: bonding temperature, bearing pressure, and bonding time, as illustrated in Figure 2. Therefore, predicting the deformation of a new design is quite challenging because of the non-linear impact of both bearing pressure and temperature [38,39]. In the DB process, the components are fixed and heated to reach the desired bonding temperature. Then, the pressure is applied and raised to the bonding pressure. Both the welding temperature and bonding pressure are maintained at a constant level throughout the holding time of the bonding process. Following the holding time, the pressure is typically lowered to its initial value to fix the samples (see Figure 2), and the temperature is reduced gradually to room temperature. The bonding temperature, time, and applied pressure have been illustrated in various literature works [36–44]. Fick's first law [45] can be implemented to describe the DB process as follows:

$$D = D_0 e^{-\frac{Q}{RT}} \quad (1)$$

where  $D$ ,  $D_0$ ,  $R$ , and  $Q$  are the diffusivity at temperature  $T$ , the frequency factor, the gas constant, and the activation energy, respectively.

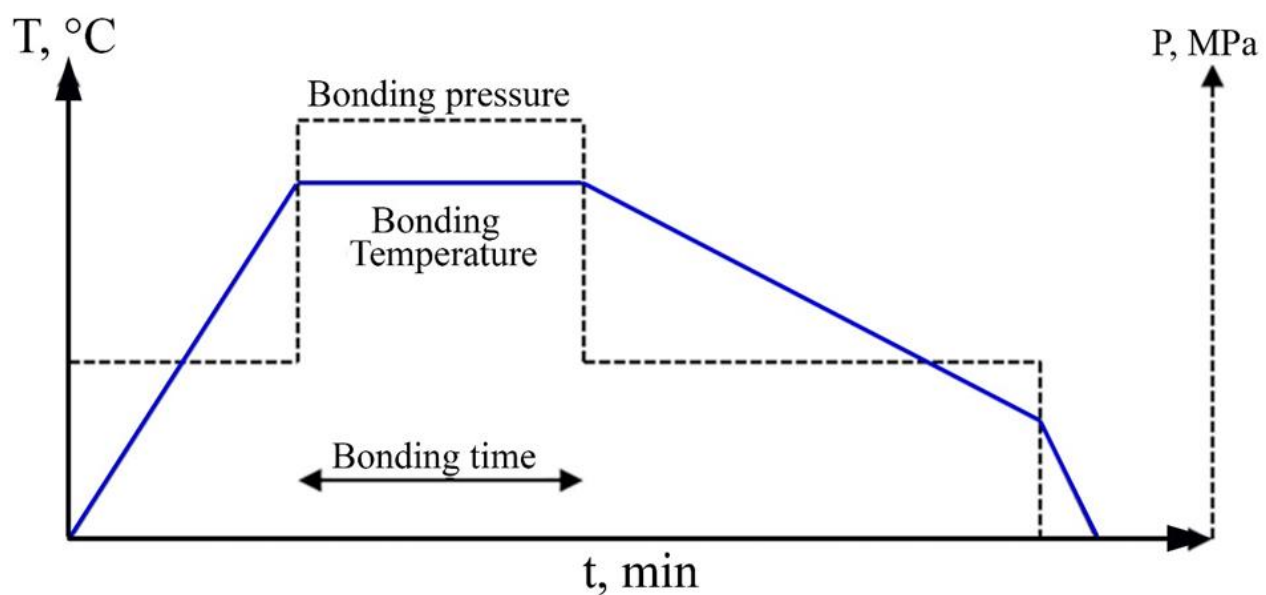


**Figure 2.** Overview of the reported parameters of the diffusion bonding process: bonding temperature, bonding pressure, and bonding time [45].

Atomic diffusion usually occurs between faying surfaces before the DB temperature is reached and similarly still occurs as the sample cools.

It is well established that the mechanism of solid-state bonding of alloys is divided into six stages, as illustrated in Figure 3. In the first stage (A), the two surfaces are in contact since better direct contact between two surfaces depends on the physical parameters related to the contact surfaces, such as irregularity, clearness, roughness, and surface treatment. In the second stage (B), DB is induced by applying microplastic deformation at the interface. Consequently, voids will form and align at the interface. At subsequent stage (C), the temperature increases to absorb the gas inside voids. The fourth stage (D) includes void shrinkage at the interface due to diffusion creep. In the fifth stage (E), the voids smaller than the critical size are unstable and will disappear rapidly. In the final stage (F), a free-void interface without discontinuity at the bonding interface is promoted. Interestingly, the bonding interface can be microscopically distinguished as a straight line.

During the last two stages, the interfacial grain boundaries migrate out of the joint plane to the lower-energy equilibrium. As the boundaries move, the remaining voids are absorbed within the grains, where they are no longer in contact with a grain boundary. Diffusion processes and creep/super-plasticity move atoms from adjacent areas to the void surfaces, decreasing the volume of interfacial voids.

Eventually, if satisfactory time is permitted, the voids will be eliminated through volume diffusion, and the atom-to-atom bond across the original interface will form during the third stage. However, the bonding does not contain melting or gross macroscopic interface distortion; thus, the bond area microstructure is like that of the areas remote from the joint and has the properties of the parent metal [46,47].

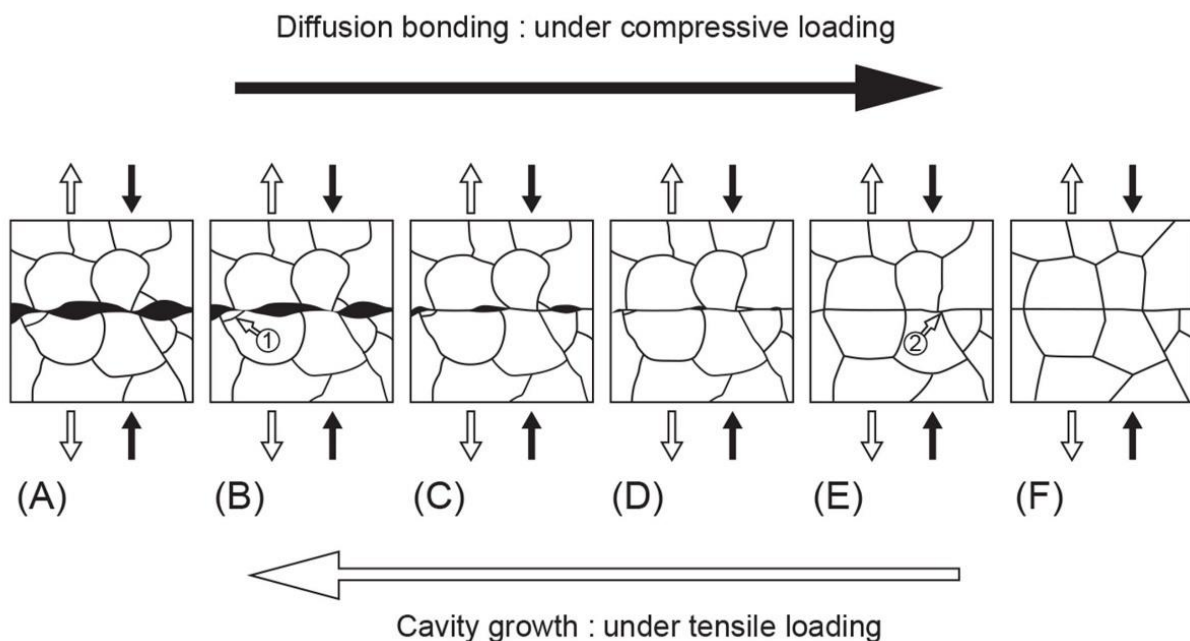


**Figure 3.** Schematic illustration of the solid-state diffusion bonding stages: (A) the first stage: surface contact, (B) the second stage: onset of diffusion bonding, (C) the third stage: evacuation of gases from the voids, (D) the fourth stage: voids shrinkage, (E) the fifth stage: voids elimination, and (F) the sixth stage: formation of a voids-free interface [47].

#### 2.1.1.1. DB of Steels

Duplex stainless steel is utilized in numerous industries, including gas and oil, petrochemicals, paper and pulp, and pollution control. Austenite stainless steel is utilized in severe and mildly corrosive environments. The fusion welding of austenitic stainless steel is typically a part of a system with low-temperature toughness and reduced corrosion resistance; consequently, it represents a limiting factor in material applications. The heat of fusion welding can cause grain coarsening in the heat-affected zone (HAZ), in addition to solidification cracking in the stainless-steel welded metal.

Compared to previous challenges, DB does not involve melting or gross macroscopic interface distortion. In addition, the lack of a fused zone in DB welding is attractive to alloys prone to segregation effects.

Kurt [34] investigated the DB of austenitic and duplex stainless steel to medium-carbon steel. Figure 4a shows the microstructure of the bonding interface between the medium-carbon steel AISI 4140 and duplex stainless steel, which displays good bonding along the interface without discontinuities or microcracks. Four distinct zones could be observed in the microstructure of the bonded dissimilar joint. Zone (I) shows the microstructure of the base metal carbon steel AISI 4140 that exhibits a ferrite-pearlite structure, Zone (II) is a ferrite stabilized region on the carbon steel side, Zone (III) shows a carbide network in

the stainless-steel side, and zone (IV) displays the microstructure of the other base metal duplex stainless steel, ferrite-austenite.

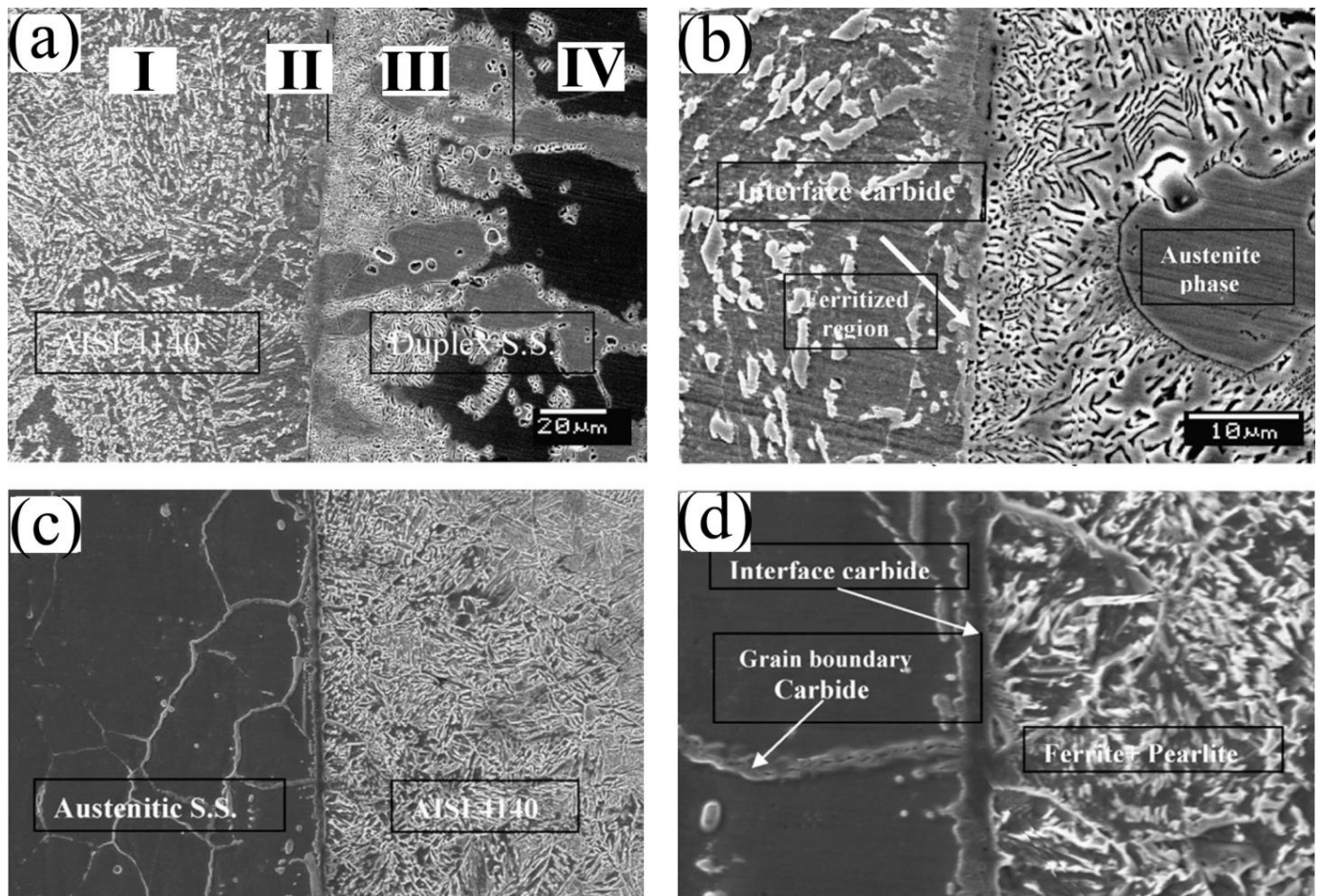


**Figure 4.** Microstructure of the bonding interface of medium-carbon steel AISI 4140 with a duplex stainless steel (a,b) and 304 austenitic stainless steel (c,d) showing: (a) defect-free interface, (b) carbide network in the stainless-steel side and carbide in the interface, (c) sound bounding interface, and (d) carbide forming on the interface [34].

Figure 4b reveals a network of carbide on the stainless-steel side and a layer of chromium-carbide on the interface. The diffusion of carbon into duplex stainless steel caused the formation of chromium-carbide around austenite grains in the ferrite phase. Carbon diffused more slowly in austenite than in the ferrite phase. Thus, carbon diffused longer in the ferrite phase, and the carbon atoms left the ferritic structure and bonded to Cr when it cooled. The Cr in carbon steel stabilized the ferrite phase and resulted in the formation of ferrite and spheroidized cementite, as depicted in Figure 4c. It was reported that adding Cr by only 0.4 wt.% of Cr to steel stabilized the ferrite in the two-phase region [48].

On the other hand, regarding the interface microstructure of the bonded medium-carbon steel and austenitic stainless-steel joint, Figure 4c,d also exhibit respectable bonding along the bonded joint's interface. Moreover, the interface was free of micro-voids and discontinuities. However, at the grain boundaries and interface region of austenitic stainless steel, the chromium carbide formed by diffusing C from the medium-carbon steel side. The shear strength of the bonded duplex stainless steel/medium-carbon steel was 767 MPa; however, the austenitic stainless steel/-medium-carbon steel joint recorded 475 MPa. Such variation can be attributed to the interface carbide amount and the ferritized zone width toward the medium-carbon steel side. As can be seen in Figure 4, the interface carbide

width in the medium-carbon steel/austenitic stainless-steel joint is higher than that in the medium-carbon steel joint.

Zhang et al. [49] studied the bonding time effect on the martensitic stainless-steel joint quality. It was found that as time increases, the large voids in the bonding interface become smaller, resulting in an increase in the interface bonding ratio.

HUO Yu et al. [50] studied the effect of the post-weld heat-treatment process and DB time on the microstructural and mechanical properties of the diffusion-affected zone by carrying out a DB test in a vacuum between dissimilar materials: TP347H austenitic heat-resistant steel and high-Cr ferrite heat-resistant steel. It was revealed that the interfacial bonding rate increased progressively when the DB time was increased. In addition, dynamic recrystallization occurred because of the interaction between the deformation storage energy difference and dislocation slip and the fine grains generated at the diffused bonding interface, which formed a serrated interface.

Moreover, Noh and Kasada [51] investigated the solid-state DB at temperatures ranging from 950 °C to 1300 °C and under a pressure of 25 MPa through a high-vacuum hot press of high Cr-ODS ferritic steel. The results showed that a defect-free joint could be obtained at a temperature of 1200 °C and a bonding time of 1 h. The bonding proved ineffective below 1200 °C due to the presence of chromium carbide and micro-voids. When bonding times were less than one hour, a creep-deformed layer and chromium carbide inclusions were detected at the bonded interface.

For simplicity, in the DB process, macroscopic deformations on the order of a few percent may occur due to high compression stress and testing temperatures. The three stages of the DB process can be used to explain how surface evolutions affect bond conditions. In the first stage, the rough surface can deform under stress before heating, resulting in an increase in the contact area. Thus, the deformation processes lead to the collapse of the surface asperities producing a network of sealed pores at the interface before the bonding continues via diffusion-controlled mechanisms such as grain boundary diffusion and power law creep [52].

The second stage involves the softer steel interface experiencing substantial deformation as the temperature increases, resulting in the voids disappearing as well as the initial asperity collapsing, thus resulting in fully intimate contact of the surfaces. It is worth noting that the final structure of the bond line depends on the composition of the surface of the pore and its interior environment. Clean, oxide-free surfaces could produce an ideal line-type bond [52]. Eventually, the final stage involves atomic diffusion at a constant temperature, and this diffusion mechanism is in line with Derby's theoretical model [53]. Possible mechanisms for DB were identified by this model, which includes: (1) plastic deformation of surface asperities, (2) power law creep deformation of the surface, and (3) diffusion of matter from interfacial void surfaces/bonded regions to growing necks [52].

Wang and Xiu [54] investigated the welding temperature impact of vacuum DB on the evolution of microstructure, interfacial morphology, and mechanical properties of AISI 304 austenite stainless steel and Q235A mild steel. Their results demonstrated that the carbon-enriched and single ferrite layers were formed near the bonding interface of AISI 304 austenite stainless steel and Q235A mild steel. In addition, on both sides of the interface, a heterogeneous microstructure was detected, and common grain boundaries were formed by diffusion. Moreover, the peak toughness and strength of the bonded joint were revealed at an approximate 850 °C welding temperature, 10 MPa welding pressure, and 60 min of welding time, which was higher than the Q235A mild-steel layer. They also demonstrated that the Cr<sub>23</sub>C<sub>6</sub> carbide formed easily at a moderately low temperature (800 °C), whereas the intermetallic compounds and secondary carbide phases formed at a higher temperature (900 °C). Thus, in both cases, forming such a carbide dramatically reduced the bonded joint's strength and toughness. Thus, in their study, they proposed to effectively avoid the formation of brittle precipitate phases by keeping the welding temperature around 850 °C, thereby ensuring the bonded joint's performance.

Kurt et al. [55] investigated the influence of the bonding temperature on the microstructural features and shear strength of austenitic stainless steel (AISI 304) and medium-carbon steel (AISI 4140) joined by DB. Figure 5 shows the SEM graphs of the diffusion-coupled interface microstructures at four different temperatures: 750, 800, 850, and 900 °C. The SEM graphs demonstrated good bonding along the bonded joint's interface at all temperatures. However, there was no considerable microstructural change at 750 °C, as there was no significant diffusion of elements, and only faying surface asperities were flattened. At 850 °C, the chromium carbides were formed at the interface zone because of the diffusion of C from the AISI 4140 side. Furthermore, martensite and partially spheroidized cementite on the AISI 4140 side could be observed. Moreover, increasing the test temperature to 900 °C resulted in a higher diffusion of C, which enlarged the chromium carbide layer in the grain boundary and interface zone; see Figure 5d.

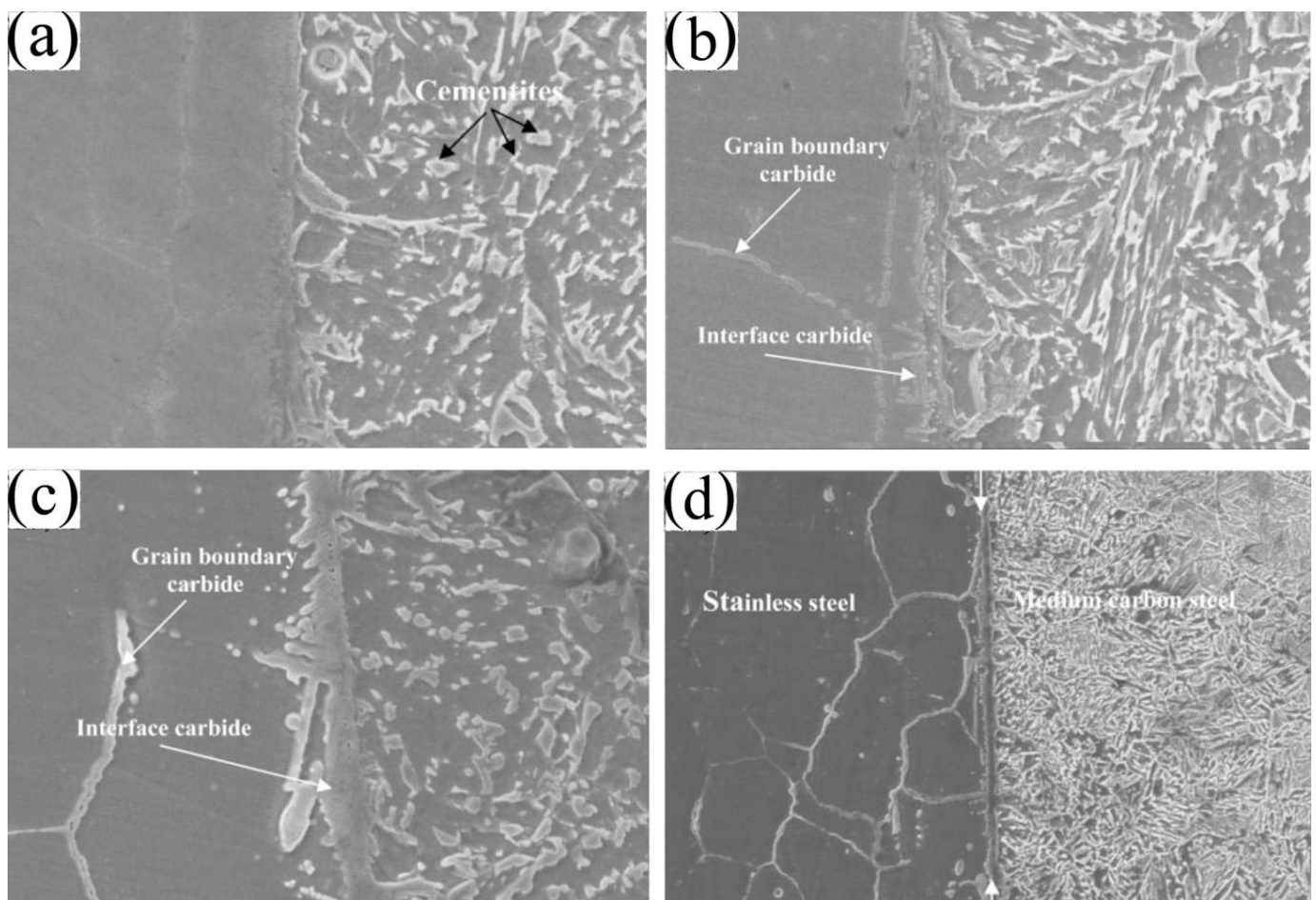


**Figure 5.** Microstructures of the bonding interface of the joints between AISI 304 austenitic stainless steel and AISI 4140 medium-carbon steel at different temperatures: (a) 750 °C, (b) 800 °C, (c) 850 °C, and (d) 900 °C [55].

Grain boundaries are considered a high-diffusion path. As a result, C diffuses into stainless steel over grain boundaries, so the carbide grain boundaries were formed, as seen in the EDS analysis (Figure 5d). As revealed by EDS analysis, the chemistry of these zones comprises of 5.9 Ni, 10.8 C, 20.8 Cr, and 62.3 Fe (in wt.%). It is well established that Cr and Fe have a significant tendency to form  $M_3C$  carbides in steel as predicted by the Isopleth equilibrium phase diagram of the system Fe–Cr–C [56]. Figure 6 displays the bonding temperature effect on both the shear strength and hardness of the joints. The joint shear strength increased with the increase in temperature because of the higher mutual diffusion of the constituents to reach its maximum value of 475 MPa at a temperature

of 900 °C; see Figure 6a. However, the martensite absence at the interface resulted in a decrease in hardness at the interface zone between AISI 4140 and AISI 304 steel, as seen in the microhardness profiles; see Figure 6b. The hardness decreased in the interface region of the carbon steel side at all temperatures, which is attributed to the diffused chromium, as shown in Figure 5d. Cr develops a ferrite-stabilized zone, thus inhibiting martensite formation.

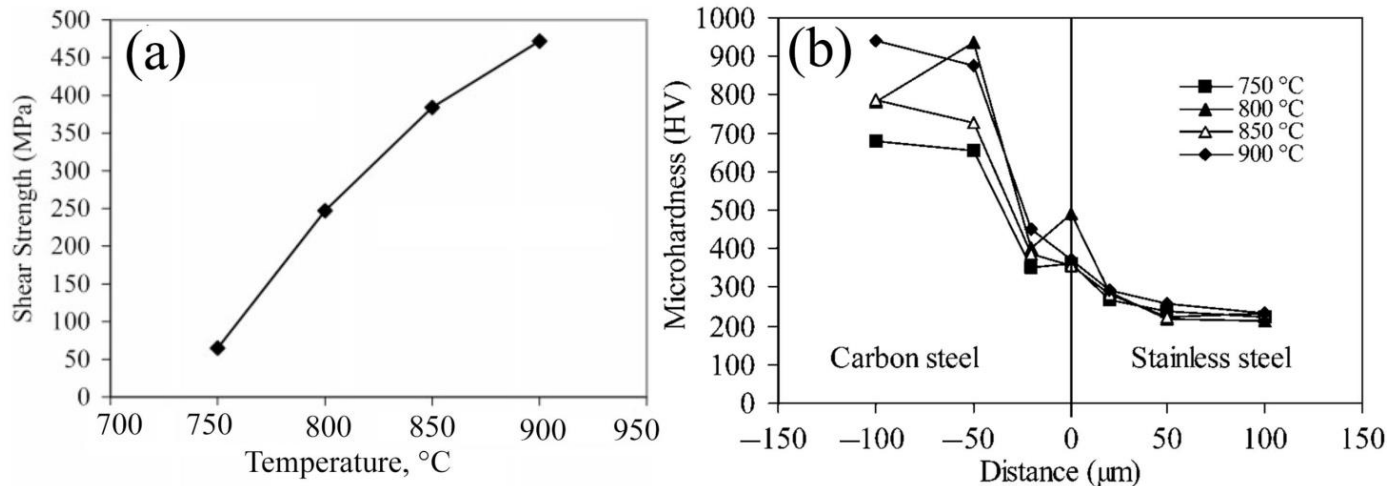


**Figure 6.** (a) The effect of bonding temperatures on compressive shear strength of the bonds, and (b) microhardness profiles of diffusion bonded interface [55].

### 2.1.2. Defects in Diffusion Bonding Two-Dimensional Defects

Two-dimensional defects of the metallic lattice include phases and grain boundaries. These defects can affect the DB. Firstly, the dislocation movement is restricted by the grain size; therefore, the grain boundaries are considered obstacles for dislocations to move through the lattice. Consequently, at constant strain, the deformation caused by the dislocation movement is slighter for the material with a small grain size. In the DB process, the applied temperature experienced by the interface region can cause a coarsening of the grain, resulting in softening behavior at the faying surfaces. Second, deformation at high temperatures is characterized by grain boundary sliding, coble creep, or vacancy flow through the volume (Nabarro–Herring creep) [57,58]. Thus, the coarse-grained material will experience a larger deformation through DB due to fewer obstacles to dislocation movement and the tendency of grains to slide against each other. Therefore, the grain size and the applied temperature are two important factors that can govern the deformation degree and the creep rate during DB.

### Three-Dimensional Defects (Precipitation)

Dissimilar metal welds of steels represent a model for local precipitation and coupled long-range diffusion occurring during DB. The most extensively investigated dissimilar metal welds are those among two ferrite steels [59,60] with dissimilar chromium contents, in addition to those between austenite stainless steel and low-alloy ferrite steel [61,62]. Moreover, it was revealed that in the similar carbon content of both steels, carbon was diffused to the high-alloyed side from the low-alloyed side [63]. Therefore, in steel metallurgy, carbon is essential, and its distribution has an essential influence on their mechanical properties. In all these cases, the driving force of carbon diffusion is the activity gradient of carbon between both steels, and it cannot be defined by the concentration of carbon only. Moreover, this type of diffusion often causes substantial changes in the microstructure around the interface bonding. In addition, carbide precipitation always occurs faster in ferritic stainless steels than in austenitic ones because of the significant carbon contents; therefore, carbon solubility in the ferritic matrix becomes much lower [64].

## 2.2. Friction Stir Welding (FSW) of Steels

FSW is a technique for metal joining in the solid state (in butt or lap positions) via a rotating friction tool. The heat generated between the tool and the material leads to an extremely soft area along the interface of the joints and the friction tool. FSW was broadly applied to non-ferrous alloys, mainly aluminum alloys. Researchers were fascinated by the ability of the FSW of steels to overcome welding defects generated during fusion welding methods of steels. FSW was introduced in 1991 [65]. Later, FSW was considered an optimum choice for welding different grades of steel that possess high melting points and/or suffer from crack formation when welded by conventional fusion methods [66–68]. Furthermore, FSW is considered a clean welding technique that provides environmentally friendly joints [69], free of volumetric defects [70].

It is well known that the weld joints produced by FSW have four different zones, specifically the stirring zone (SZ); the thermo-mechanically affected zone (TMAZ), which is caused by the higher temperature and lower strain that occurs during FSW processing; the heat affected zone (HAZ); and the unaffected zone, which is known as the parent metal (PM) or base metal (BM). Specimens welded by the FSW process have HAZs smaller than the specimens joined by fusion welding. For instance, tungsten arc welding was reported to produce HAZs with great widths due to the relatively high heat input [71,72], which may result in the failure of joints created by fusion welding [73]. Comparatively, FSW generates lower heat in the HAZ. Therefore, FSW is preferred for joining steel grades sensitive to thermal cycles rather than fusion welding techniques [74]. Moreover, FSW refines the grain size in the SZ because of the severe plastic deformation carried out by the stirring tool [75], which significantly affects the strength, ductility, and toughness of the FSW joints [76]. On the one hand, during the FSW processes, C and Cr atoms were diffused through the weld metal; consequently, C/Cr-rich regions and depleted zones were formed. This may negatively affect the mechanical properties of the welded joints due to the inhomogeneous distribution of the chemical composition [77,78]. On the other hand, because of the tempered martensite formation and the refined austenite in the SZ, FSW specimens showed higher tensile strength than the specimens joined by activated-gas tungsten arc welding of 9Cr-1Mo and 316LN stainless steel [72].

The FSW process is carried out by a stirring tool that rotates between two fixed sheets or plates as butt or lap joints [79,80]. The circular tool is a non-consumable tool that rotates against the sheet/plate surface under the effect of an axial load. The tool contains a shoulder and a solid surface or threaded cylindrical pin that heats the workpiece [76]. The rotating tool is fixed in a chuck on the headstock of a milling machine or any indigenously built FSW machine. The tool geometry, travel speed, and rotational speed of the tool during FSW, therefore, directly affect the physical, mechanical, and microstructural properties of joints. Thus, increasing the tool travel speed led to lower peak temperatures and a higher strain rate in the WZ [80]. Increasing the rotational speed resulted in a substantial increase in the SZ peak temperature [71,81]. The maximum peak temperature ( $T$ ) caused in the SZ during FSW of steels can be estimated by using Equation (1) [72].

$$T = \left( \frac{\omega^2}{\vartheta \times 10^4} \right)^\alpha \times T_m \times K \quad (2)$$

where  $\omega$ ,  $\vartheta$ , and  $T_m$  are the tool rotational speed (rpm), weld travel velocity ( $\text{mm}\cdot\text{min}^{-1}$ ), and melting temperature of BM, respectively;  $K$  and  $\alpha$  are constants ( $K = 0.64$  and  $\alpha = 0.04$ ).

Furthermore, Wang et al. [82,83] presented a deeply analytical and comprehensive study of the bonding behavior under various operating conditions of the FSW process. Their model was completely different from other solid-state bonding models as they relied on the well-established knowledge of the grain boundary creep fracture of high-temperature polycrystalline materials rather than rough surface contact and volumetric inter-diffusion for interfacial gap closure (other models).

It was supposed that the interfacial cavities would shrink under the combined action of sintering and applied compressive stresses under the creep-controlled deformation or according to the Hull–Rimmer diffusive process [53]. Their model demonstrated that the solid-state bonding under FSW depends principally on the creep strain rate in the adjoining workpieces, weakly on stress triaxiality, and negligibly on interfacial diffusion. Moreover, the bonding extent increased with the increase in the tool rotational speed and plunging depth or with a decrease in the tool welding speed. The maximum bonding extent in the FSW process, as well as the maximum cladding thickness that can achieve full bonding in the FSW cladding process, was about half of the tool radius.

In the following sections, we report the microstructure evolution and mechanical properties of SZ, TMAZ, and HAZ, as well as welding defects accompanying FSW of similar and dissimilar steels. However, the tool design, material selection, and wear behavior are not included in the present study.

### 2.2.1. FSW of Similar Steels

Ghosh et al. [80] studied the lap joints of martensitic steel with high strength via M190 sheets with a 1 mm thickness containing 0.19C-0.47Mn-0.17Si, produced by FSW using diverse cooling rates and heat input. The BM of the welded joints had a martensite microstructure; however, the SZ structure varied according to the cooling rate associated with the welding parameters. A slow cooling rate promoted the formation of a ferrite–pearlite structure, while a rapid cooling rate led to the formation of a martensite structure in the weld zone. Moreover, it was found that the HAZ represents the weakest region of all joints and consists of ferrite structure in addition to slight pearlite quantities, which reduced hardness values compared with the SZ. Consequently, during the shear testing, the welded joints fractured along the HAZ.

Ragab et al. [84,85] carried out the FSW of lap joints between martensitic steel sheets with high strength and a thickness of 3.8 mm. The tool used in the FSW process was made of W-25%Re and had a tapered threaded pin with a length of 2.95 mm and a 3 mm tip pin diameter. The traverse speed of the tool was 75 mm/min and was kept constant, the tool rotational speeds ranged between 250 rpm and 650 rpm, and the SZ was basin-shaped. Their results revealed that the BM microstructure consists of quenched martensite laths with small amounts of M23C6 carbides. Moreover, the peak temperature was achieved at a rotational speed of 550 rpm; therefore, the required temperature for transforming austenite to delta ferrite was reached. The width of the HAZ increased with the increase in the tool's rotational speed. The microstructure of the SZ was recrystallized dynamically, and the fine martensite laths were formed. The M23C6 carbides disappeared in the SZ. At 250 rpm in the SZ, the grain size of the prior austenite grain was 43% of the BM, and the size of martensite was about 68% of the BM. A further increase in the speed of the tool to 550 rpm resulted in an additional increase in prior austenite and martensite to 68% and 87% of the BM, respectively. The grain refinement was attributed to the CDRX effect. Furthermore, the SZ and TMAZ recorded the greatest values of the average hardness and rose 20% to 25% compared to the hardness of BM. However, the lowest hardness values were recorded in the HAZ, and they were 80% at the lowest rpm and 75% at the highest rpm compared to the BM.

Further increase in tool rotation to 650 rpm resulted in the fill lack defect due to excessive heat input. At high temperatures, the steel at the weld surface showed a tendency toward decohesion. Therefore, the tool shoulder was insufficient to form and constrain the plasticized weld metal.

Wang et al. [74] performed FSW on the lap joint of DP1180 (dual-phase structures of martensite and ferrite) with three different tool-tip diameters (0.2, 0.4, and 0.8 mm) at 400 rpm and a 150 mm/min traverse speed. The composition of the used DP1180 steel is presented in Table 1. The findings showed that the microstructure consisted of a typical dual-phase structure of martensite and ferrite. The tempered martensite phase formed in the SZ because the temperature during the FSW exceeded the Ac<sub>3</sub>. The stability of the

present phases in the HAZ was slightly affected by the increasing temperature since it showed the existence of the tempered martensite phase, which was surrounded by fine ferrite. The tempered martensite and soft ferrite formation were the major reason for hardness reduction in the HAZ. The HAZ was subdivided into three zones according to the size of the ferrite phase. The further the distance from the stirring zone, the larger the ferrite size. Additionally, they reported that when the stirring pin was increased from 0.4 to 0.8 mm, the joint shear strength was decreased due to the formation of intermittent veins as the material was piled slightly on the surface of the rear weld.

**Table 1.** DP1180 steel chemical composition (wt.%) [74].

C	Mn	Si	Cr	Mo	Cu	Al	S	P	Fe
0.18	2.4	0.60	0.02	0.01	0.02	0.05	0.005	0.01	Bal.

Wang et al. [86,87] studied the weldability of quenched and partitioned advanced high-strength 1180 steel via the FSW technique. Table 2 presents the chemical composition of the QP1180 steel sheets. The sheets had thicknesses of 1.6 mm. FSW was processed at two different rotational velocities, 450 and 600 rpm. Figure 7 shows three regions of the HAZ at two different rotational velocities. Moving away from the SZ, the HAZ was categorized as fine-grained HAZ (visible only for the welded joints at 600rpm), which was experienced at a temperature that reached Ac3; inter-critical HAZ (IC-HAZ), which was experienced at a temperature that ranged between Ac3 and Ac1; and sub-critical HAZ (SC-HAZ) which was subjected to a temperature below Ac1. It is worth noting that, for this steel, the Ac1 and Ac3 temperatures of phase transformation are 746 °C and 847 °C, respectively [88]. In addition, the width of the HAZ was improved with the rotational velocity of the stirring tool increase. The PM showed a dual-phase microstructure of ferrite (F) and lath martensite. The SZ showed a microstructure of full martensite. The formed martensite at 600 rpm showed coarser grains compared to that formed at 450 rpm. In addition, the structure of the fine-grained HAZ was like the SZ. The IC-HAZ and SC-HAZ showed a dual-phase structure of martensite and ferrite. In their results, it was found that the HAZ was softer than the SZ and PM. Hardness reduction in HAZs was attributed to the gradual fraction growth of ferrite. The welded joint tensile strengths were equal to the PM, while the ductility decreased. Moreover, joints welded at 600 rpm showed failure during the tension test in the HAZ.

**Table 2.** QP1180 steel chemical composition (wt.%) [86,87].

C	Mn	Si	Al	S	P	Fe
0.19	2.76	1.60	0.039	0.003	0.01	Bal.

Johnson et al. [89,90] investigated the weldability of AISI 321 stainless steel sheets (3 mm thick) via FSW. Table 3 shows the AISI 321 steel chemical composition. The welding process was conducted at a 55 mm/min traverse speed, 500 and 700 rpm tool rotational rates, 13 KN axial force, and a 1.5° tool tilt angle. It was revealed that the PM exhibited an austenitic structure. In the weld SZ, the microstructural structures exhibit that the evolution of the structure of equiaxed, fine austenite grains was dominated by a discontinuous dynamic recrystallization mechanism. Consequently, the hardness at the SZ was significantly higher compared to the BM hardness.

**Table 3.** QP1180 steel chemical composition (wt.%) [89,90].

Grade	C	Mn	Si	P	S	Cr	Ni	N
321	0.04	2.00	0.75	0.045	0.030	18	10.5	0.10

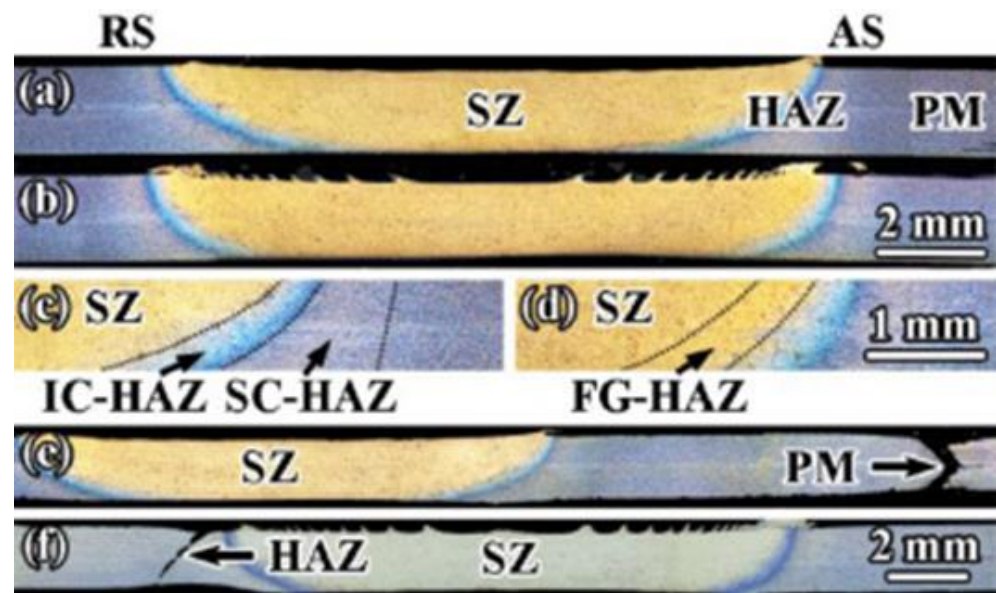


Figure 7. Cross-sectional views of FSW at 450 rpm (a,c,e) and 600 rpm (b,d,f) [86].

The maximum microhardness, 245 HV, resulted from welding at a speed of 75 mm/min, which was revealed in the weld SZ. However, the yield strength of the base steel was 320 mPa, and the yield strength of the welded joints was 555 at a welding speed of 500 rpm and 579 mPa at 700 rpm. In addition, the ultimate tensile strength of the welded joints was recorded at 610 mPa at a welding speed of 500 rpm, while the UTS increased to 632 mPa at 700 rpm. The ductility of the weld joints was lower than the BM; however, the dimple structure was detected at the fracture zones.

Kumar et al. [86] studied the impact of the FSW tool material on the microstructural and mechanical properties of the 316L stainless-steel butt-welded joints. Table 4 shows the 316L stainless steel chemical composition. The sheets had thicknesses of 1.6 mm each. The study implied the usage of two different tools: a tungsten lanthanum oxide and a tungsten heavy alloy tool. The FSW was carried out using a 600 rpm tool rotational speed and 45 mm/min welding speed. The results showed that the tungsten lanthanum oxide tool produced joints with improved microstructural and mechanical behavior compared to the joints processed by the tool made of the tungsten heavy alloy.

Table 4. 316L stainless steel chemical composition [91].

Element	C	Mn	S	P	Si	Ni	Cr	N	Mo	Fe
% by wt.	0.02	0.8	0.004	0.04	0.28	10.07	16.58	0.035	2.02	Bal

Figure 8 illustrates the optical and SEM micrographs of the 316L BM. The BM showed the existence of an austenite matrix in addition to low amounts of ferrite. In addition, annealing twins were found, at some locations, crossing grain boundaries. In addition, the average grain size was  $25 \pm 4 \mu\text{m}$ . However, after the FSW using the tungsten lanthanum oxide tool, in the SZ, roughly equiaxed grains with  $7 \pm 3 \mu\text{m}$  average grain sizes were formed, as can be seen in Figure 9. On the other hand, FSW using the tungsten heavy alloy tool resulted in an appearance of equiaxed and ultra-fine grains with  $6 \pm 3 \mu\text{m}$  average grain sizes in the SZ. The sigma phase was not detected in any zone in the interface region of the joint. In addition, the average grain sizes in the TMAZ of joints produced by tungsten lanthanum oxide and tungsten heavy alloy tools were  $10 \pm 3$  and  $8 \pm 3 \mu\text{m}$ , respectively. The yield strength of joints produced by both tools was significantly greater than the BM due to the grain refinement in the SZ, as well as the hardness increased across the joint (as

shown in Table 5). The sigma phase was not indicated in either case in any region of the interface joint zone.

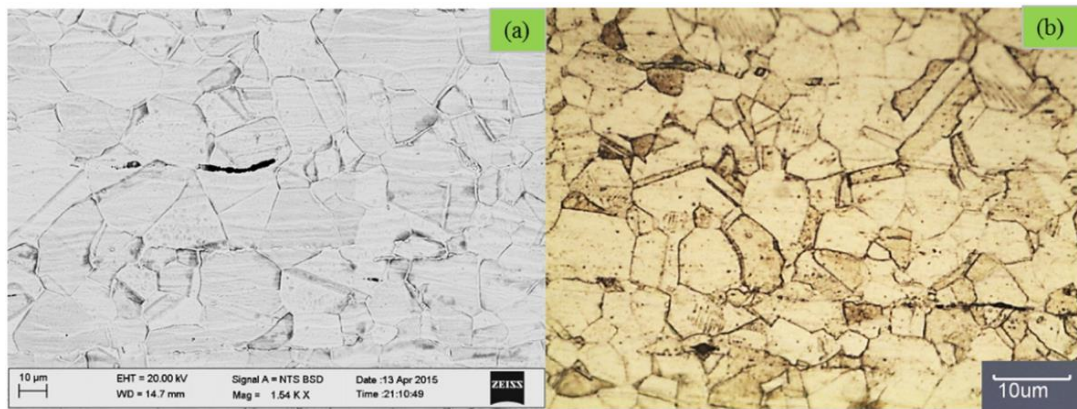


Figure 8. As-received AISI 316L base metal micrographs: (a) SEM, (b) OM [91].

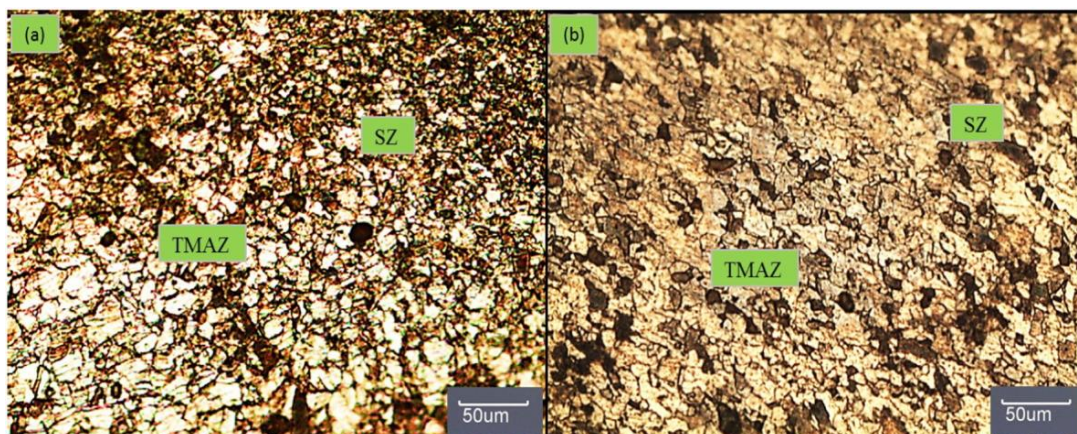


Figure 9. Different zones along the advancing side of the joint produced using (a) tungsten lanthanum oxide tool and (b) tungsten heavy alloy tool [91].

Table 5. Mechanical properties of 316L stainless steel welded joints [91].

Condition	Yield Strength, mPa	Ultimate Tensile Strength, mPa	Percentage Elongation, %	Joint Efficiency, %
Base metal	320 ± 4	630 ± 6	55 ± 1	–
FSW joint processed via W-1% La <sub>2</sub> O <sub>3</sub> tool	381 ± 7	609 ± 8	31 ± 4	96 ± 1.3
FSW joint processed via tungsten heavy alloy tool	362 ± 5	542 ± 6	19 ± 3	86 ± 1

Additionally, Ramesh et al. [92] used the FSW technique to weld 3 mm-thick 316L ASS plates. The microstructure and mechanical behavior of the studied welding conditions were reported. The chemical composition of the investigated 316L ASS plates is listed in Table 6. In their study, a tungsten alloy (W-Re) tool was utilized for the FSW. Varied traverse speeds were used and ranged from 45 mm/min to 85 mm/min, with a step of 10 mm/min at 500 RPM. No tool wear was recorded [92]. The findings of their investigation showed

that the BM exhibited coarse austenitic grains, as well as several annealing twins inside the grains. The SZ displayed significant grain refinement, as well as XRD confirmation of the presence of delta ferrite phase traces at 45–65 mm/min traverse speeds. The twin plate volume fraction was reduced in the SZ. The grains in the SZ were equiaxed. Moreover, the grain size decreased as the traverse speed increased. Grain refinement occurred due to dynamic recrystallization during FSW. On the other hand, the TMAZ showed slightly elongated grains, and the HAZ showed a similar structure to the PM.

**Table 6.** 316L ASS chemical composition [92].

Element	C	Si	Mn	P	S	Cr	Ni	Mo	Al	Cu	Ti	Fe
wt.%	0.033	0.332	1.18	0.0150	0.014	17.510	9.01	0.259	0.019	0.540	0.294	Balance

In their study, the PM and SZ showed hardness values of  $160 \pm 5$  and  $190 \pm 15$ , respectively. The SZ displayed higher hardness compared to the parent metal under all FSW conditions due to grain refinement. The hardness values increased as the traverse speed increased due to grain size reduction, decreasing the degree of deformation at higher traverse speeds, thus reducing the density of the existing dislocations in the SZ. Moreover, the joint strength and fracture toughness improved with an increase in traverse speed from 45 to 65 mm/min, then decreased because of the existence of root flaws above the 65 mm/min traverse speed. It is worth noting that insignificant root defects existed at the plate at 75 and 85 mm/min traverse speeds, while these defects did not appear at 45, 55, and 65 mm/min traverse speeds.

Sunilkumar et al. [77,81] carried out FSW of 9Cr-1Mo steel butt joints at 200 and 500 rpm. Each sheet had a 3 mm thickness. It was found that the BM microstructure of the 9Cr-1Mo steel consisted of tempered martensitic within the prior austenite grain boundary with a  $12 \pm 2 \mu\text{m}$  average grain size. It was revealed that, at a 200 rpm tool rotational speed, the peak temperature was lesser than the lower critical transformation temperature (Ac1). Regarding the 200 rpm weld, fine martensite was detected in the SZ, which was attributed to the significant plastic deformation through FSW and the high hardenability of the 9Cr-1Mo steel. Nevertheless, the peak temperature was between Ac3 and Ac1 when using a tool rotational speed of 500 rpm. The SZ showed a typical lath martensitic structure. Using 200 rpm exposed comparatively higher hardness at the SZ (about 20 VHN) compared to 500 rpm, which was attributed to the formation of a fine-grained structure. Their results revealed that the grain size of the base metal was  $\sim 12 \mu\text{m}$ . The distribution of the grain size between the weld SZ matrix of the specimen displayed a finer grain size of  $\sim 4 \mu\text{m}$  at 200 rpm compared to the 500 rpm weld, which was  $\sim 5.9 \mu\text{m}$ . This is attributed to the higher dynamic recrystallization effect at 200 rpm compared to 500 rpm.

Kumar et al. [93] applied FSW to join 3 mm of AISI 316L stainless steel at butt joints. The AISI 316L stainless steel chemical composition is shown in Table 7. The FSW tool was made from a tungsten-lanthanum alloy (99% W, 1% La<sub>2</sub>O<sub>3</sub>). The welding process was conducted at a 600 rpm tool rotational speed, 12 kN axial force, and a 1.5° tool tilt angle. Different welding speeds ranged from 25 mm/min to 100 mm/min, with 25 mm/min increments.

**Table 7.** AISI 316L stainless steel chemical composition of tested elements [93].

Element	C	Mn	S	P	Si	Ni	Cr	N	Mo	Fe
wt.%	0.02	0.8	0.004	0.04	0.28	12.07	16.58	0.035	2.02	Bal

The results revealed that the base steel microstructure demonstrated coarse grains of austenite and minor amounts of ferrite. The base steel had an average grain size of  $28 \pm 5 \mu\text{m}$ . The austenitic matrix decreased as the welding speed increased, and the average grain size in the SZ decreased from 142 at 25 mm/min, to 72 at 50 mm/min, and 32 at

75 mm/min. Moreover, the equiaxed grains in the SZ were clearly indicated due to the discontinuous dynamic recrystallization mechanism during FSW. In addition, the highest temperatures in the welded joints were 1164, 975, and 798 °C at 25, 50, and 75 mm/min, respectively. Moreover, low welding speeds resulted in the formation of a delta ferrite phase in the SZ. The delta ferrite phase emerged as a thin flake-like structure between the austenite grain boundaries. Additionally, the ferrite phase fraction in the SZ was  $7.21 \pm 0.45\%$ . However, in the TMAZ, the average grain size produced using different welding speeds of 25, 50, and 75 mm/min was  $16 \pm 2$ ,  $10 \pm 2$ , and  $7 \pm 2$   $\mu\text{m}$ , respectively. Consequently, welding speed significantly impacted the microstructural evolution in the WZ, toughness, and joint strength. The welded joint fracture toughness improved as the welding speed increased. The toughness and tensile strength using a welding speed of 75 mm/min were 49 J/cm<sup>2</sup> and 632 MPa, respectively, whereas the toughness and tensile strength of the BM were 50 J/cm<sup>2</sup> and 630 MPa, respectively. The BM recorded a hardness value of  $190 \pm 5$  HV. Furthermore, the highest microhardness, 275 HV, was recorded in the SZ when welded using 75 mm/min as the welding speed. Thus, the microhardness at the SZ increased with the increase in welding speed, which was attributed to the growth of fine equiaxed grains. The presence of austenite fine equiaxed grains and the consequent hardness improvement at the SZ caused the superior strength of the joint compared to steel processed at higher welding speeds. However, exceeding the welding speed limit resulted in a lack of material coalescence and plasticization, which led to defects in the internal tunnel.

Sekban et al. [94] joined low-carbon steel plates (ASTM 131A) by FSW. The sheets (4 mm thickness each) contain wt.% of 0.16C-0.18Si, 0.7Mn, 0.11S, 0.18P, 0.09Cr, 0.14Mo, 0.04Cu, 0.04V, and a balance of Fe in their chemical composition. The tool's rotational speed was 630 rpm, and the traverse speed was 45 mm/minutes. In addition, the tilt angle of the shoulder was 3 deg, with 11 kN of downforce during the FSW process. The results demonstrated that the PM contained coarse grains of ferrite and pearlite phases, and the ferrite phase had an average grain size of about 25  $\mu\text{m}$ , as shown in Figure 10. Micrographs of the FSWed joint microstructure are presented in Figure 11. The microstructure of the SZ consisted of an equiaxed fine-grained microstructure because of the dynamic recrystallization. Moreover, the ferritic grain size decreased in the SZ from 25  $\mu\text{m}$  to approximately 4  $\mu\text{m}$ . In addition, during FSW, the SZ temperature was above the A3 temperature line. No martensitic or bainitic transformation occurred in the welding area during the FSW. However, the upper side of the welded zone, which made direct contact with the tool shoulder, showed the existence of martensite and bainite phases because of the higher cooling rate in comparison with the deeper SZ material. The nearest zone of the HAZ to the SZ showed fine-grained ferrite and perlite, while the middle area of the HAZ exposed refined pearlite colonies and a small fraction of the ferrite grains. In addition, the nearest part of the HAZ showed ferrite grains and spheroidized carbide. The differences in the structure of the HAZ are attributed to the variations in the temperature profile during the FSW technique.

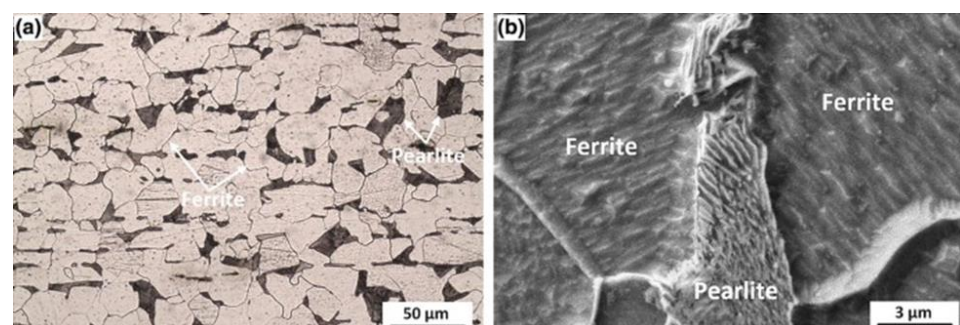


**Figure 10.** Steel-plate coarse-grained microstructures (a) via OM and (b) via SEM, showing ferrite and pearlite phases morphologies [94].

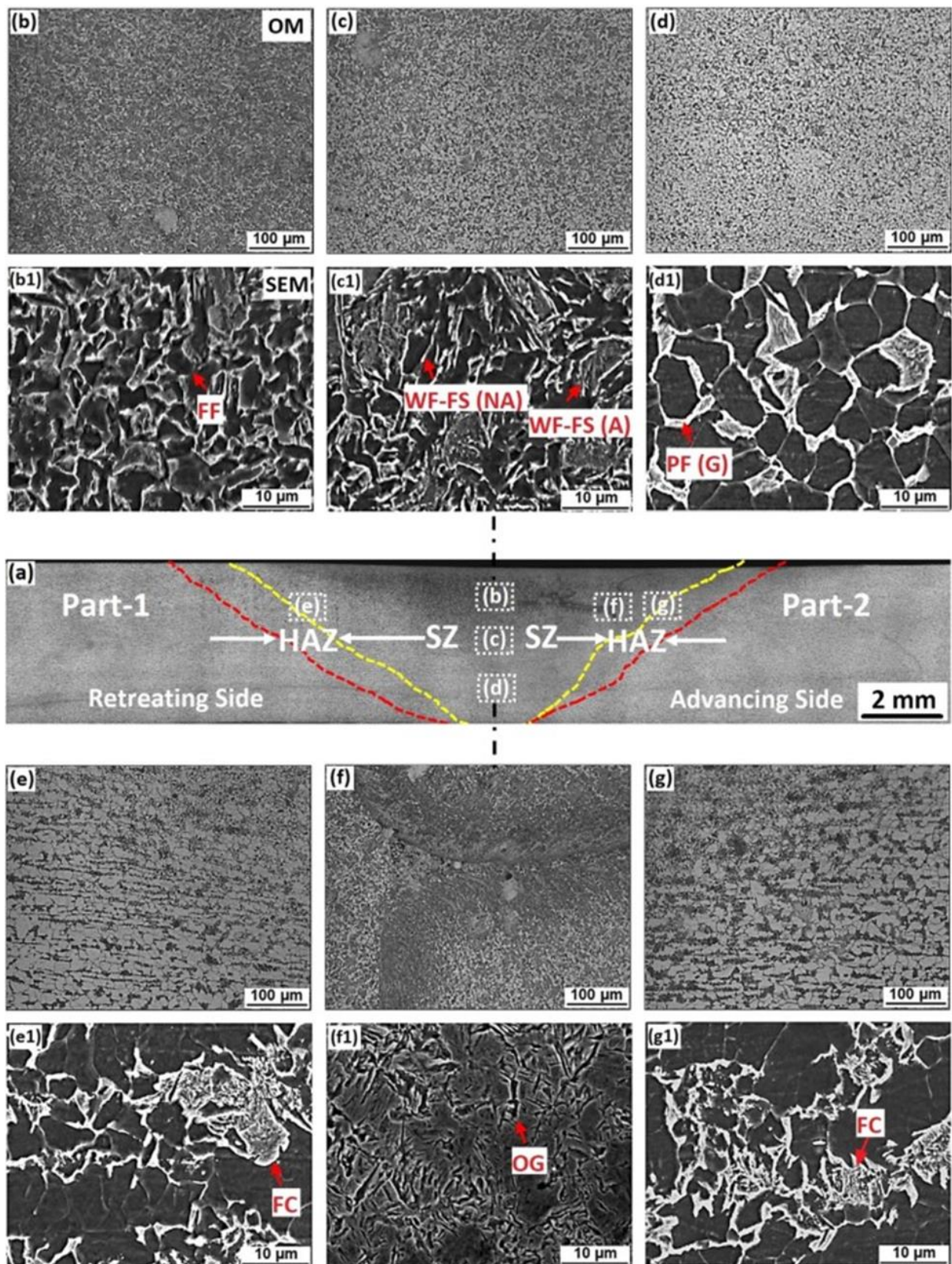


**Figure 11.** Microstructure of FSWed joints showing: (a) a cross-sectional view of the welded joint, (b,b1) the shoulder-effected SZ, (c–d1) the SZ from the top of the surface through the subsurface, (e,e1) the transition region on the retreating side, (f,f1) the region with oriented and fine-grained 316L stainless steel, and (g,g1) the transition region on the advancing side [94].

The dynamic recrystallization in the SZ occurred because of the significant plastic deformation; thus, the Widmanstatten ferrite structure generated a moderately low dislocation density. Shear bands of subgrains were perpendicularly oriented to the Widmanstatten ferrite plates because of intensive plastic deformation, as shown in Figure 12a. Figure 12b reveals the ferrite-cementite aggregates. The lamellae cementite in the initial microstructure, perlite, is fragmented by the rotating pin stirring effect. Additionally, the SZ hardness rose from 140 to approximately 230 Hv0.3. Moreover, the SZ yield strength increased from 256 to 435 MPa, whereas the tensile strength rose from 457 to 585 mPa without significantly decreasing the ductility.

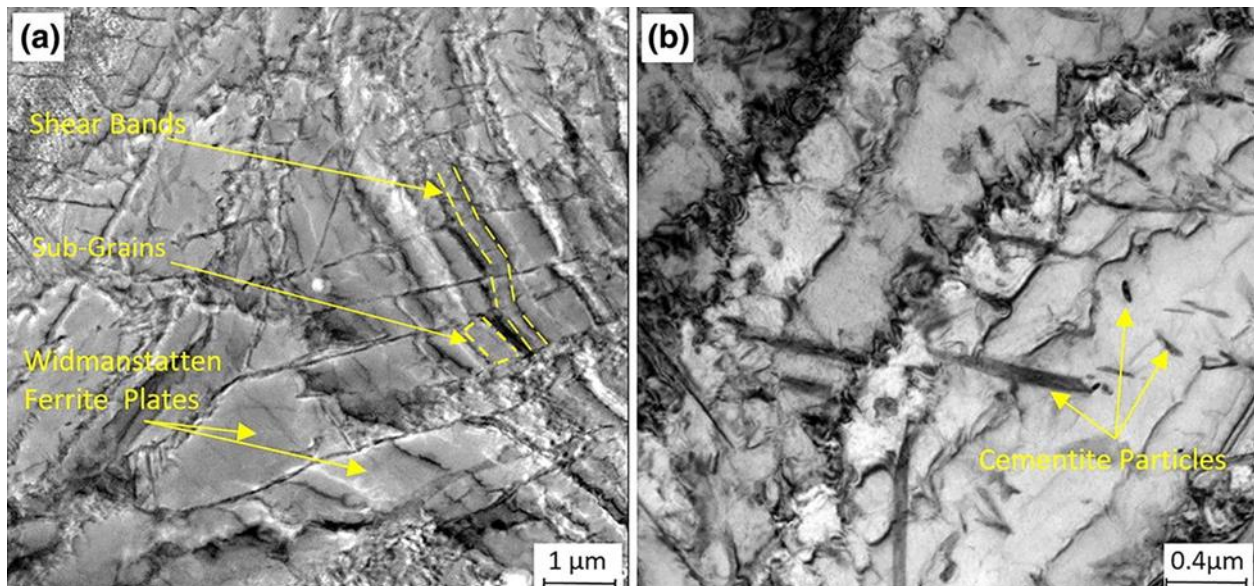


**Figure 12.** TEM micrographs at the SZ of the joint structure. (a) Widmanstatten ferrite with shear bands and (b) ferrite-cementite aggregates (FC) with sub-grains formed by dislocations [94].

Kamaraj et al. [95] joined HSLA steel sheets (3mm thickness each) through FSW. The FSW was carried out by a tungsten-rhenium tool at 500 rpm. The traverse speed was diverse from 57 to 97 mm/min with 10 mm/min in step. In their work, the PM microstructure showed the existence of pearlite and ferrite. During FSW, the peak temperature was greater than the allotropic transformation temperature ( $A_3$ ) at the different traverse speeds (57, 67, and 77 mm/min), while it was lower than 600 °C at 87 and 97 mm/min. Furthermore, the weld nugget microstructure exposed the upper bainite phase and the presence of fine ferrite. The traverse speed reduced the amount of upper bainite, as revealed by EBSD, which can be attributed to the peak temperature decrease and the rapid cooling rate. In addition, the grain size decreased with the traverse speed increase.

The weld nugget exhibited higher hardness than the refined ferrite and bainite phases. However, the hardness decreased with the faster traverse speed, which can be attributed to the bainite structure formation reduction and the soft ferrite phase increase.

Furthermore, the strength of the joint at 57 mm/min was 540 MPa, and at 97 mm/min was 407 MPa. A traverse speed below 78 mm/min resulted in a higher strength because of the hard weld nugget. However, an additional increase in the traverse speed led to lower joint strength, which can be attributed to macroscopic defects and poor consolidation. The macroscopic defect-forming tendency increased with the increase in traverse speed; this resulted in a tensile strength reduction. Groove defects and root flaws were detected at a 97 mm/min traverse speed. In addition, using 97 mm/min as the traverse speed did not pass the root bend test.

### 2.2.2. FSW of Dissimilar Steels

In this regard, Sauraw et al. [96] used an FSW technique to join different grades of Cr-Mo steel, modified 9Cr-1Mo: P91, and 2.25Cr-1Mo: P22 for application in a power plant. The chemical compositions of the base plates are presented in Table 8. The FSW of 2.25Cr-1Mo to 9Cr-1Mo steel was performed on a square butt geometry under 200 and 500 rpm. The ERNiCrMo-3 Ni-based superalloy was utilized as a filler material.

**Table 8.** Chemical compositions of P91 and P22 base plates [96].

Elements	C	Mn	P	S	Si	Ni	Cr	Mo	Fe
P9 steel, wt. %	0.12	0.502	0.020	0.0008	0.50	0.20	8.80	0.95	Bal.
P22 steel, wt. %	0.14	0.50	0.020	0.002	0.30	0.20	2.18	0.92	Bal.

The PM microstructure of the 9Cr-1Mo steel consists of tempered martensitic within prior austenite grain boundaries with an average grain size of  $12 \pm 2 \mu\text{m}$ . In contrast, the 2.25Cr-1Mo steel exhibited ferritic–bainitic phases in the microstructure with an average grain size of  $15 \pm 3 \mu\text{m}$ . Additionally, in their study, the SZ microstructure revealed the existence of a martensitic structure, and the peak temperature evolution at the SZ was above the Ac1. Hence, tempered martensite/bainitic and the proeutectoid/ferrite structure of 9Cr-1Mo-2.25Cr-1Mo BM were changed to a single-austenite phase during the FSW process heating cycle and then transformed to martensite by the progressive cooling cycle. The EBSD results confirmed the increase in low-angle grain boundaries in the SZ with the rotational speed increase from 200 rpm to 500 rpm due to the increase in the dislocation numbers related to severe plastic deformation from the FSW process. The TMAZ of FSW-processed 2.25Cr-1Mo and 9Cr-1Mo sides revealed a typical lath martensitic structure. The severe plastic deformation associated with FSW induced the martensitic phase transformation while increasing the tool’s rotational speed increased the martensite lath size.

Moreover, the HAZ microstructure of the 9Cr-1Mo side exposed a fine martensitic structure; however, the 2.25Cr-1Mo side of the microstructure consisted of ferrite, bainite, and tempered bainitic structures. The ferrite structure was coarsened with an increase in the rotational speed of the tool from 200 rpm to 500 rpm, which can be attributed to the slow cooling rate at higher heat input. Eventually, the hardness of the SZ, TMAZ, and HAZ of the specimens welded by FSW was higher than other specimens welded by TIG. However, the ductility of the specimens joined by FSW was lower than those welded by TIG after a post-heat treatment was applied. Thus, FSW is not recommended for welding steel grades that require post-weld heat treatments due to the existence of a soft zone and hard zone in the weld zone.

Sunilkumar et al. [72] investigated the microstructure evolution and mechanical properties of welded 316LN stainless steel to 9Cr-1Mo (P9) steel via FSW. The FSW was performed with a tool rotational speed of 400 and 600 rpm and 3 mm-thick butt joints. It was found that at 600 rpm, tool wear was recognized. The parent metal microstructure of the 9Cr-1Mo steel revealed a tempered, martensitic microstructure within the prior austenite grain boundary; the average grain size was  $12 \pm 2 \mu\text{m}$ . The parent metal microstructure of the 316LN SS showed an equiaxed austenitic structure in addition to annealing twins. Furthermore, the average grain size was  $23 \pm 5 \mu\text{m}$ . Figure 13 shows the structure of the joined 9Cr-1Mo and 316LN. The matrix interface (SZ) of the dissimilar weld had a martensitic structure and refined austenite because of dynamic recrystallization. The evolved peak temperature of 9Cr-1Mo steel during the FSW was near the Ac3 temperature, and the 9Cr-Mo side microstructure had lath martensite. Additionally, the austenite deformed grains were detected in the TMAZ of the 316LN side, while the HAZ of the 316LN side showed finer austenitic grains. However, on the 316LN side, the HAZ was four times wider than the HAZ of the 9Cr-1Mo side due to its higher thermal conductivity. Joints produced by FSW showed higher strength and ductility than those produced by TIG. Nevertheless,

the HAZ width of the specimens welded by FSW was approximately half the value of the HAZ width of the specimens welded by TIG.

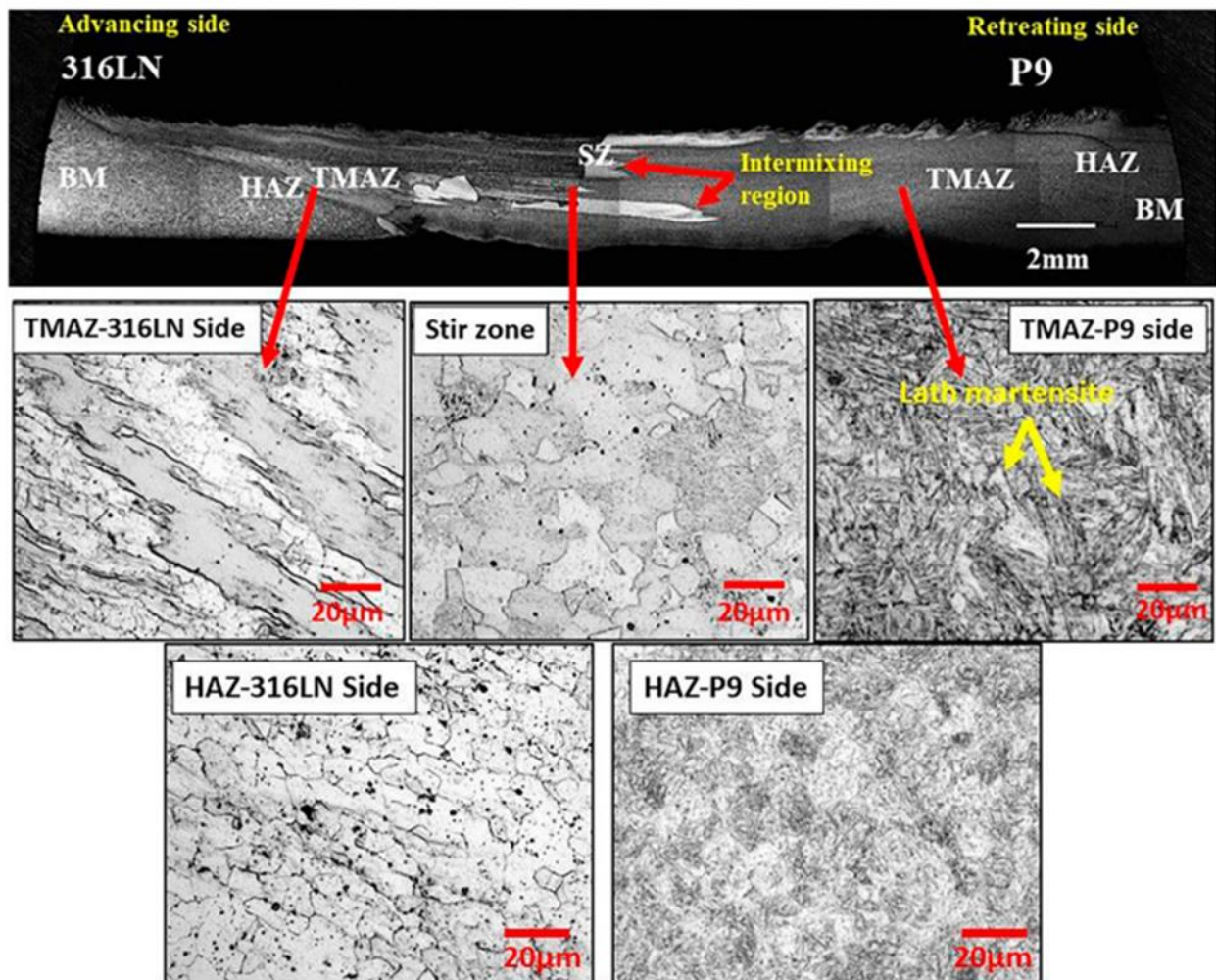


**Figure 13.** Cross-sectional microscopic view of FSW weldments [72].

Rahimi et al. [97] implemented FSW to join 2205 duplex stainless steel to S275 low-carbon-manganese structural steel sheets (butt joints, 6 mm thickness each). The FSW was performed at a tool rotational speed of 200 rpm and 100 mm/min traverse speed, under 55 kN as the average downward axial force, and 0.6 mm offset toward the Duplex steel. The BM of the S275 low-carbon steel contained equiaxed ferrite grains and pearlite colonies with an average grain size of 10.3  $\mu\text{m}$ . The BM of the duplex steel contained austenite islands embedded in the ferrite matrix with 4.2 and 5.8  $\mu\text{m}$  average grain sizes.

The results revealed that the grain refinement of the ferrite and austenite phases was achieved at the TMAZ and SZ in the duplex stainless steel and the S275 steel. The grain refinement was attributed to the dynamic recrystallization of the austenite and ferrite phases. On the one hand, discontinuous dynamic recrystallization was activated at the original austenite/austenite grain boundaries in the duplex stainless steel. On the other hand, continuous dynamic recrystallization was promoted in the ferrite phases of both duplex stainless steel and S275 steels.

The estimated temperature during FSW welding in the SZ center reached a temperature between AC3 and AC1. Both ferrite and austenite fraction changes in the duplex stainless steel were recorded. Furthermore, the generated heating cycle by the FSW moderately transformed the original SZ BM microstructure of S275 steel, ferritic-pearlitic, to the dual-phase state of austenite-ferrite at temperatures directly above the Ac1. Further, the

heating resulted in a minor phase transformation of ferrite to austenite in the S275 steel. Furthermore, the temperatures induced during the FSW process resulted in the formation of a mixed microstructure mainly consisting of polygonal ferrite, in addition to a minor acicular ferrite fraction in the SZ because of the transformation of austenite-ferrite during cooling. Additionally, in both steels, grain refinement resulted in an insignificant increase in the hardness of the TMAZs.

Wang et al. [98] performed FSW for joining 2205 duplex stainless steel, UNS S32205, and 304 austenitic stainless steel, UNS S30400. The duplex stainless steel sheet had a 1.86 mm thickness, while the austenitic stainless steel sheet had a 1.89 mm thickness. The FSW was performed using the WRe25 tool at a rotational speed of 400 rpm and a 50 mm/min transverse speed. The welding was carried out at offsets with distances of 1 mm and 0 mm, and each steel was alternately placed in the RS and AS.

The results showed that the BM of the duplex stainless steel contained austenite and ferrite with average grain sizes of 3 and 3.7  $\mu\text{m}$ , respectively. The austenitic stainless steel BM contained an austenite phase with an average grain size of 17  $\mu\text{m}$ . After FSW, the SZ of the duplex stainless steel showed very fine grain sizes of austenite and ferrite ranging from 0.5 to 1.6  $\mu\text{m}$ , while the SZ of the austenitic stainless steel showed a refined austenite grain size of 2.6  $\mu\text{m}$ . Additionally, the welded joint hardness was higher than the BMs because of the dynamic recrystallization through welding. The austenitic stainless steel hardness at the SZ increased from 210 HV to 250 HV. Moreover, the duplex stainless steel hardness increased from 265 HV to 330 HV. The tensile specimens were fractured at the 304 BM.

The mixing of material when positioning 304 ASS on the advancing side (AS) showed better performance compared to the position of the opposite material; also, the distribution of hardness in the SZ was more uniform. Nevertheless, when positioning 304 austenitic stainless steel on the AS, the SZ width was greater than that of the opposite material's position because of the higher strength of the 304 ASS compared to the 2205 DSS at the welding temperature.

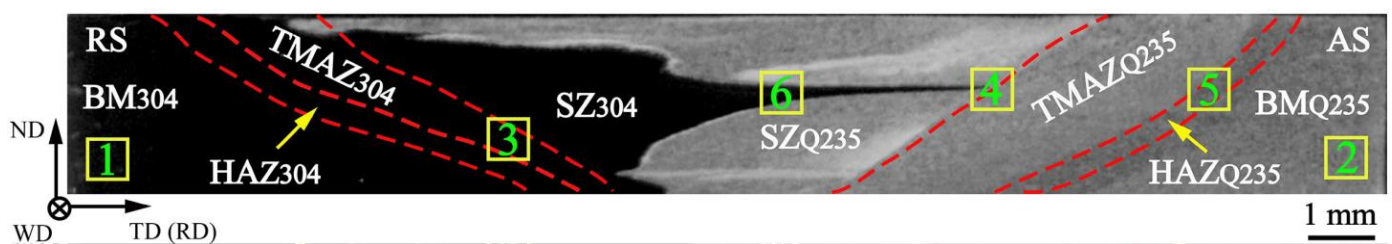
Venkatakrishna et al. [76] carried out FSW for 9Cr-1Mo-V-Nb to 316 L (N) butt joints (each sheet had a 3 mm thickness). The tool's rotational and traverse speeds were 400 rpm and 60 mm/min, respectively. The BM of the 9Cr-1Mo-V-Nb steel had a microstructure consisting of prior austenite with a  $28.61 \pm 3.62 \mu\text{m}$  average grain size and lath martensite, while 316 L (N) steel had a microstructure of austenite with a  $60.21 \pm 5.4 \mu\text{m}$  average size. During FSW, the welding temperature reached 931  $^{\circ}\text{C}$ , and the cooling rate was approximately 16.75  $^{\circ}\text{C}/\text{s}$ . It was revealed that the SZ showed a refined austenite structure and tempered martensite due to continuous dynamic recrystallization and severe shearing action during the FSW process. It is worth mentioning that the SZ was free from  $\delta$  ferrite formation. The TMAZ and HAZ showed refined structures on both sides. The existence of refined austenite and tempered martensite enhanced the mechanical behavior of the FSW joints when compared to activated tungsten inert gas and/or laser-beam welding. The 316L (N) and 9Cr-1Mo-V-Nb steels had hardness values of  $246 \pm 16 \text{ HV}$  and  $197 \pm 21 \text{ HV}$ , respectively. The SZ recorded hardness values ranging from 301 to 351 HV. In addition, the welded joints displayed a UTS of 634 MPa, which fell between the UTS of the 316L (N) and 9Cr-1Mo-V-Nb steels, 619 MPa and 687 MPa, respectively. Moreover, the dissimilar joint yield strength was recorded at 298 MPa, which was considered an intermediate value that fell between those of the joined base plates (431 and 290 MPa). Additionally, the ductility of the welded joints was 42%, which was between that of the BMs (18 and 62%). Further, the impact toughness of the welded joints was 41 J, which was between those of the BMs (22 and 53 J).

Wang et al. [78] conducted a dissimilar FSW of Q235 low-carbon steel to 304 austenitic stainless steel at butt joints of 3 mm thickness each. Table 9 illustrates the present elements and their weight% in welded 304 steel and Q235 plates. The FSW was performed by a WC-Co tool consisting of a pin shape with six truncated pyramids and a cylindrical shoulder. The rotational speed during FSW was 475 rpm, with a welding speed of 47.5 mm/min. The 304 steel and Q235 plates were positioned on the retreating side (RS) and AS, respectively.

**Table 9.** Base metal chemical compositions (wt.%) [78].

Steel	C	Mn	Si	Cr	Ni	Mo	V	Cu	P	S	Fe
SS304	0.058	0.712	0.501	17.975	8.348	0.005	0.115	0.049	0.034	0.005	Bal.
Q235	0.167	0.284	0.162	0.0186	0.0042	0.001	0.0011	0.0037	0.0205	0.0096	Bal.

The BM of the 304SS contained austenite with a 10.9  $\mu\text{m}$  average grain size, whereas the BM of the Q235 steel contained ferrite and pearlite. The pearlite lamellar structure was located at the boundaries of ferrite grains. The ferrite had a 5.7  $\mu\text{m}$  average grain size. Figure 14 shows the dissimilar FSW joint macrostructure of Q235 and SS304 steels. After FSW, the SZ of the 304SS side showed a refined austenitic structure with a 5.5  $\mu\text{m}$  average grain size due to the discontinuous dynamic recrystallization effect.

**Figure 14.** Cross-sectional macrostructure of FSW joint of dissimilar SS304 and Q235 steels [78].

The results demonstrated that the SZ of the Q235 steel showed a combination of proeutectoid ferrite and pearlite phases; the ferrite had a 7.3  $\mu\text{m}$  average grain size. The coarsening of the ferrite phase was attributed to the FSW-process-induced temperature. The welding temperature ranged between 947 and 1074  $^{\circ}\text{C}$ , which was greater than the  $A_{c3}$  (austenitizing temperature) of the Q235 steel. The grain coarsening was attributed to pearlite coarsening induced by the temperature increase. The TMAZ showed grain refinement on the 304 side, while the grain size of the ferrite phase in the TMAZ was 8  $\mu\text{m}$  on the Q234 side. The acicular ferrite amount was decreased. The HAZ was only subjected to a thermal cycle, so the HAZ showed grain coarsening on the 304 SS side while the fraction of LAGBs increased due to the occurrence of dynamic recovery. The ferrite grain size was 6  $\mu\text{m}$  in the HAZ in the Q234 side.

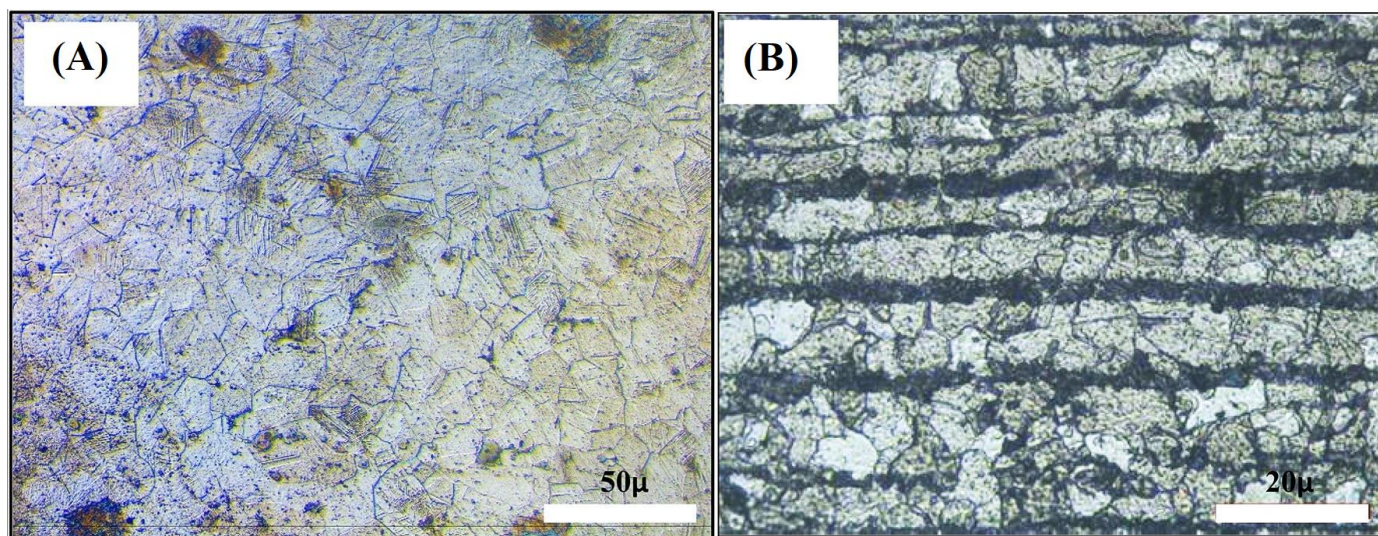
On the other hand, the average BM microhardness values were 210 and 154 HV in the 304 SS and Q235 steel, respectively. The hardness of the welded joints (SZ, TMAZ, and HAZ) was increased on the two sides. However, the maximum microhardness, 325 HV, appeared on the SZ upper surface of the Q235 side due to the migration of Cr atoms from the 304 SS side to the Q235 steel side. Additionally, the FSW joint tensile strength was 493 MPa, which fell between the UTS of the two steels. The fracture was not located in the SS304 and Q235 low-carbon steel interface. It was instead located at the SZ of the Q235 steel, which indicates the higher strength of the interfacial bonding. However, the welded-joint elongation was lesser than the elongation of the two steels.

Matlan et al. [99] performed FSW for stainless steel 316 and low C-steel by double-sided butt joints, the chemical composition of the joined steels is displayed in Table 10. The sheets each had a 10 mm thickness. The FSW was carried out with a 100 mm/min traveling speed and 500 and 1000 rpm tool rotational speed in combination with preheating temperatures of 50 and 100  $^{\circ}\text{C}$ . The FSW tool was made of a composite material, W-Re-HfC, with a 20 mm shoulder, a truncated cone pin with a 5 mm tip pin diameter, and an 8 mm end pin diameter with a pin length of 5 mm.

**Table 10.** 316 SS and low CS chemical composition [99].

Element	C	Si	Mn	P	S	Ni	Cr	Mo	Cu	N	Ti	Al	Nb
316 SS	0.08	0.4	0.83	0.018	0.001	10.1	16.2	2.1	0.3	0.06	-	-	0.03
CS	0.18	0.36	1.2	0.018	0.002	0.23	0.04	0.004	0.21	0.004	0.005	0.031	-

The AISI 316 stainless steel was located on the weld AS, and the low C-steel was on the weld RS. The FSW was carried out in argon shielding gas to prevent surface oxidation of the weld metal. The BM of the 316 SS has an austenitic microstructure, while the BM microstructure of the C-steel has a mixed microstructure of equiaxed ferrite grains and pearlite colonies, as displayed in Figure 15.

**Figure 15.** Micrographs of (A) AISI 316 SS and (B) low-carbon steel [99].

Their results demonstrated grain refinement in the two steels after FSW. No HAZ was observed in stainless steel. The joint interface demonstrated a complex swirl-like shape linked to the stirring flow path, while the flow lines, such as the onion ring structures, were not observed in the SZ. It was revealed that a thin layer of carbon steel material was stirred to the TMAZ of the stainless steel side. The use of a rotational speed of 1000 rpm and pre-heating at 50 °C displayed the greatest brittle behavior because of the micro-void formation in the brittle and hard phases in the weld zone. The length of the voids varied from 20 μm to 100 μm with a thickness of approximately 1–2 μm. During the U-Bend test, a crack a few millimeters in length was revealed in the TMAZ of the stainless steel section. Further, the specimens pre-heated at 50 °C and then welded at 1000 rpm exposed the presence of voids near the TMAZ of the stainless steel section.

Tiwari et al. [100] also carried out FSW for welding butt joints of stainless steel, UNS S30400, and mild steel, UNS G10080. The sheets had a 4 mm thickness. The FSW was achieved using a tungsten carbide tool with rotational speeds of 600 and 875 rpm and tool offsets of 0.6 and 1.2 mm. The tool offset/eccentricity was executed by moving the tool towards the mild steel side; see Figure 16. Tool wear occurred under different mechanisms (adhesion, abrasion, and oxidation wear). Tungsten particles were found in the SZ, which was detrimental to the weld joint impact strength. The BMs were mild steel (UNS S10080) and stainless steel (UNS 30400).

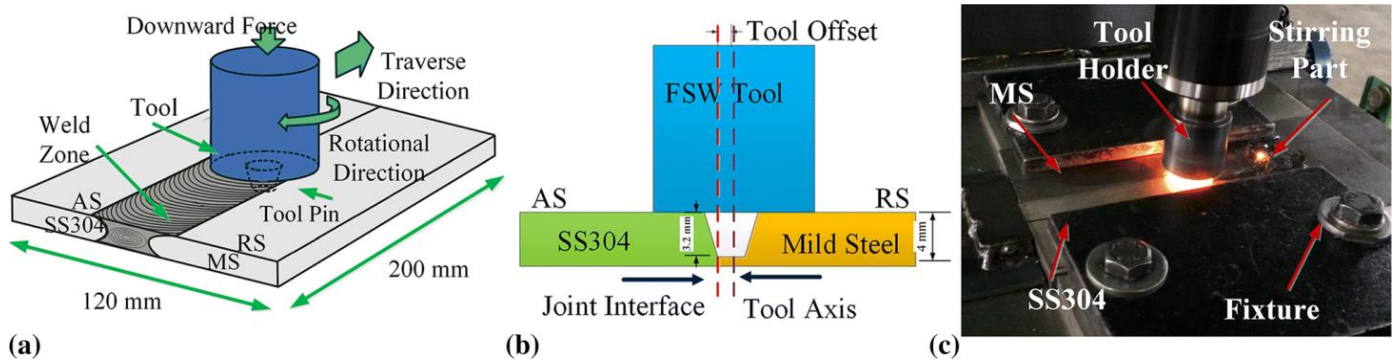


**Figure 16.** (a) Schematic drawing of dissimilar FSW butt joints, (b) tool offset toward the softer material, mild steel, and (c) FSW of SS304 and MS in progress [100].

The results showed that the microstructure of SS304 and mild steel mainly consisted of the ferrite phase. However, the SS304 displayed higher tensile strength, percentage elongation, hardness, and fracture toughness compared to the mild steel. The SZ demonstrated the existence of ferrite, austenite, and carbide precipitates, as revealed by XRD. Moreover, the SZ showed large Ni and Cr peaks in the SS304-rich regions; thus, the MS region decreased, as revealed by EDS. Additionally, it was found that the joints' YS and UTS increased with an increase in the tool offset distance and rotational speed. The increases in the UTS of the welded joints in SS304 and mild steel are attributed to the grain size and strengthening of phase transformation, respectively. However, the elongation to failure was 9.6%, which was a decline of 53.8% compared to the mild steel. In addition, it was found that the welded joints had lower ductility and fracture toughness than the base metals. Significant tool wear was observed, which negatively affected the mechanical properties.

On the other hand, the microhardness of mild steel BM and stainless-steel BM was about 88 HV<sub>0.5</sub> and 149 HV<sub>0.5</sub>, respectively. The maximum hardness of the mild steel side ranged from 121 to 129 HV in SZ, from 95 to 102 HV in the HAZ, and from 106 to 116 HV in the TMAZ, which was attributed to microstructure refinement. The SZ with Widmanstätten ferrite and acicular ferrite structures had a maximum hardness of 281 HV<sub>0.5</sub>. The hardness values in the SZ and TMAZ of the welds were extremely ununiform because of the mixed complex material in the weld zone.

Ipekoğlu et al. [101] conducted FSW of dissimilar low-carbon steel sheets with different carbon fractions of 0.17 and 0.25 wt.%, St37 and St52, respectively. The FSW was processed using a tungsten carbide tool. During the FSW process, the tool traverse speed and rotational rate were constant at 65 mm/min and 630 rpm, respectively. The BMs showed a mixed structure of pearlite and ferrite with different grain sizes of ferrite; the volume fractions of the pearlite phase were 9% and 18% in the St37 and St52, respectively. After FSW, the SZ showed a mixed structure of Widmanstätten ferrite, either ferrite with or without carbide aggregates. The low cooling rate in the SZ resulted in the appearance of the Widmanstätten ferrite phase. Moreover, the severe plastic deformation in the SZ led to pearlite phase dissolution. The HAZ was composed of fine pearlite grains, fine equiaxed ferrite grains, and coarse ferrite grains.

Additionally, the BM showed hardness values equal to 180 HV in St52 and 137 in St37, respectively. However, the hardness of the SZ reached 347 HV due to grain refinement and solid-state transformation. The welded plates showed a UTS of 389 MPa, thus lying between the UTS of St37 (373 MPa) and St52 (526 MPa). Furthermore, the dissimilar joints recorded a yield strength of 272 MPa, which was also an intermediate value and fell between those of the joined base plates. The welded joint elongation reached 9%, which was lower than the ductility of St37 and St52 (45 and 35, respectively). The low ductility was attributed to the existence of Widmanstätten ferrite and/or cementite aggregates in the SZ.

### 3. Conclusions

This paper reviewed the solid-state welding of steels using two different techniques, DB and FSW. The solid-state welding techniques and their microstructure evolution when applied to steel were briefly reviewed.

Considering DB, the following conclusions have been drawn from the above survey:

1. The DB between dissimilar steels, such as duplex stainless and austenitic stainless steel with medium-carbon steel, was significantly sound in promoting a defect-free interface.
2. The microstructural evolution at the bonding interface between dissimilar steels showed carbide precipitation. Consequently, the bonding interface promotes a higher mechanical strength than the base metals. The characteristics of the bonding interface are affected by different aging parameters, such as temperature and time.
3. Principally, FSW processing of steels promotes the grain structure of the different zones in the joint and grain refinement to the microscale of the TMAZ and SZ structure. Consequently, the mechanical strength of the joint is enhanced.
4. The heat generation during FSW processing of steels affects the microstructure of the joints, for instance, tempering of martensitic steel, inducing a second phase ( $\delta$ -ferrite) in austenitic structure, forming upper bainite carbon steels, and forming lath martensite due to fast cooling from a temperature above  $A_{c1}$ .
5. Inappropriate heat input results in the appearance of weld defects. With the increase in heat input, a lack-of-fill defect is formed, and decohesion at the weld surface is noticed due to the high-temperature effect.

**Author Contributions:** Conceptualization, M.K., A.H. and W.A.-E.; Investigation, M.K., A.H. and W.A.-E.; writing—original draft preparation, M.K. and W.A.-E.; writing—review and editing, M.K., A.H., A.J., S.E. and W.A.-E.; Supervision, A.H.; funding acquisition, A.J. All authors have read and agreed to the published version of the manuscript.

**Funding:** This research was funded by [financial assistance of Business Finland, project FOSSA-Fossil-Free Steel Applications] grant number [5498/31/2021].

**Data Availability Statement:** Data will be made available on request.

**Acknowledgments:** The researcher Mahmoud Khedr received a full scholarship from the Ministry of Higher Education of the Arab Republic of Egypt. Atef Hamada and Antti Järvenpää would like to acknowledge financial assistance of Business Finland, project FOSSA- Fossil-Free Steel Applications. Elsevier LTD., Springer Nature LTD., and Taylor & Francis group are acknowledged for giving license permissions for reusing figures and tables.

**Conflicts of Interest:** The authors declare no potential conflicts of interest with respect to the research, authorship, and/or publication of this article.

### References

1. Wu, D.; Zhang, P.; Yu, Z.; Gao, Y.; Zhang, H.; Chen, H.; Chen, S.; Tian, Y. Progress and perspectives of in-situ optical monitoring in laser beam welding: Sensing, characterization and modeling. *J. Manuf. Process.* **2022**, *75*, 767–791. [[CrossRef](#)]
2. Bölükbaşı, Ö.; Yüksel, C. A comparative study on metallographic and mechanical properties of ArmoX 500T armor steel plates joined using different arc welding methods. *Exp. Tech.* **2022**, 1–16. [[CrossRef](#)]
3. Vaishnavan, S.S.; Jayakumar, K. Tungsten inert gas welding of two aluminum alloys using filler rods containing scandium: The role of process parameters. *Mater. Manuf. Process.* **2022**, *37*, 143–150. [[CrossRef](#)]
4. Shete, H.V.; Gite, S.D. Optimization of argon gas metal arc welding process parameters with regard to tensile strength for AISI 310 stainless steel using taguchi technique. In *International Journal of Engineering Research in Africa*; Trans Tech Publ.: Zürich, Switzerland, 2022.
5. Singh, D.K.; Sharma, V.; Basu, R.; Eskandari, M. Understanding the effect of weld parameters on the microstructures and mechanical properties in dissimilar steel welds. *Procedia Manuf.* **2019**, *35*, 986–991. [[CrossRef](#)]
6. Anawa, E.; Olabi, A.-G. Control of welding residual stress for dissimilar laser welded materials. *J. Mater. Process. Technol.* **2008**, *204*, 22–33. [[CrossRef](#)]
7. Harada, Y.; Sada, Y.; Kumai, S. Dissimilar joining of AA2024 aluminum studs and AZ80 magnesium plates by high-speed solid-state welding. *J. Mater. Process. Technol.* **2014**, *214*, 477–484. [[CrossRef](#)]

8. Ghosh, N.; Pal, P.K.; Nandi, G. GMAW dissimilar welding of AISI 409 ferritic stainless steel to AISI 316L austenitic stainless steel by using AISI 308 filler wire. *Eng. Sci. Technol. Int. J.* **2017**, *20*, 1334–1341. [[CrossRef](#)]
9. Sridharan, N.; Isheim, D.; Seidman, D.; Babu, S. Colossal super saturation of oxygen at the iron-aluminum interfaces fabricated using solid state welding. *Scr. Mater.* **2017**, *130*, 196–199. [[CrossRef](#)]
10. Kah, P.; Shrestha, M.; Martikainen, J. Trends in joining dissimilar metals by welding. In *Applied Mechanics and Materials*; Trans Tech Publ.: Zürich, Switzerland, 2014.
11. Golbabaee, F.; Khadem, M. Air pollution in welding processes—Assessment and control methods. *Curr. Air Qual. Issues* **2015**, 33–63.
12. Popović, O.; Prokić-Cvetković, R.; Burzić, M.; Lukić, U.; Beljić, B. Fume and gas emission during arc welding: Hazards and recommendation. *Renew. Sustain. Energy Rev.* **2014**, *37*, 509–516. [[CrossRef](#)]
13. Pires, I.; Quintino, L.; Miranda, R.M.; Gomes, J.F.P. Fume emissions during gas metal arc welding. *Toxicol. Env. Chem.* **2006**, *88*, 385–394. [[CrossRef](#)]
14. Kah, P.; Martikainen, J. Current trends in welding processes and materials: Improve in effectiveness. *Rev. Adv. Mater. Sci.* **2012**, *30*, 189–200.
15. Zhou, K.; Yao, P. Overview of recent advances of process analysis and quality control in resistance spot welding. *Mech. Syst. Signal Process.* **2019**, *124*, 170–198. [[CrossRef](#)]
16. Zhan, M.; Guo, K.; Yang, H. Advances and trends in plastic forming technologies for welded tubes. *Chin. J. Aeronaut.* **2016**, *29*, 305–315. [[CrossRef](#)]
17. Hu, Y.; Wu, S.; Chen, L. Review on failure behaviors of fusion welded high-strength Al alloys due to fine equiaxed zone. *Eng. Fract. Mech.* **2019**, *208*, 45–71. [[CrossRef](#)]
18. Oi, K.; Murayama, M. Recent trend of welding technology development and applications. *JFE Tech. Rep.* **2015**, *20*, 1–7.
19. Akca, E.; Gürsel, A. Solid state welding and application in aeronautical industry. *Period. Eng. Nat. Sci. PEN* **2016**, *4*, 1–8. [[CrossRef](#)]
20. Nassiri, A.; Abke, T.; Daehn, G. Investigation of melting phenomena in solid-state welding processes. *Scr. Mater.* **2019**, *168*, 61–66. [[CrossRef](#)]
21. Yildirim, S.; Kelestemur, M.H. A study on the solid-state welding of boron-doped Ni3Al–AISI 304 stainless steel couple. *Mater. Lett.* **2005**, *59*, 1134–1137. [[CrossRef](#)]
22. Koteswararao, B.; Suresh, Y.; Ravi, D. Analysis of quality in solid state welding (copper-copper) by using NDT and DT by altering physical properties at constant time. *Mater. Today Proc.* **2017**, *4*, 7351–7356.
23. El Mahallawy, N.; Fathy, A.; Abdelaziem, W.; Hassan, M. Microstructure evolution and mechanical properties of Al/Al–12% Si multilayer processed by accumulative roll bonding (ARB). *Mater. Sci. Eng. A* **2015**, *647*, 127–135. [[CrossRef](#)]
24. Mahallawy, N.E.; Fathy, A.; Hassan, M.; Abdelaziem, W. Evaluation of mechanical properties and microstructure of Al/Al–12% Si multilayer via warm accumulative roll bonding process. *J. Compos. Mater.* **2017**, 0021998317692141. [[CrossRef](#)]
25. Aleem, H.A.A. Study on Bonding of Dissimilar Metals by Ultrasonic Bonding and Materials Evaluation of the Bonds. Ph.D. Thesis, Kyushu Institute of Technology, Kitakyushu/Iizuka, Japan, 2004.
26. Ni, Z.; Ye, F. Ultrasonic spot welding of aluminum alloys: A review. *J. Manuf. Process.* **2018**, *35*, 580–594. [[CrossRef](#)]
27. Coronado, J.; Cerón, C. Fracture mechanisms of CTOD samples of submerged and flux cored arc welding. *Theor. Appl. Fract. Mech.* **2010**, *53*, 145–151. [[CrossRef](#)]
28. Brothers, D.G. The Origin of Acicular Ferrite in Gas Metal Arc and Submerged Arc Welds. Master’s Thesis, Naval Postgraduate School, Monterey, CA, USA, 1994.
29. Kreye, H. Melting phenomena in solid state welding processes. *Weld. J.* **1977**, *56*, 154–158.
30. Al-Sabur, R.K.; Jassim, A.K. Friction stir spot welding applied to weld dissimilar metals of AA1100 Al-alloy and C11000 Copper. In *IOP Conference Series: Materials Science and Engineering*; IOP Publishing: Philadelphia, PA, USA, 2018.
31. Reddy, M.G.; Rao, S.A.; Mohandas, T. Role of electroplated interlayer in continuous drive friction welding of AA6061 to AISI 304 dissimilar metals. *Sci. Technol. Weld. Join.* **2008**, *13*, 619–628. [[CrossRef](#)]
32. Miyashita, Y.; Mutoh, Y.; Akahori, M.; Okumura, H.; Nakagawa, I.; Jin-Quan, X. Laser welding of dissimilar metals aided by unsteady thermal conduction boundary element method analysis. *Weld. Int.* **2005**, *19*, 687–696. [[CrossRef](#)]
33. Abdelaziem, W.; ElMahallawy, N.; Hassan, M.; Fathy, A. Effect of wire brushing on cold roll bonding of Al 1050 sheets. *Egyptian J. Eng. Sci. Technol.* **2015**, *18*, 3–4. [[CrossRef](#)]
34. Kurt, B. The interface morphology of diffusion bonded dissimilar stainless steel and medium carbon steel couples. *J. Mater. Process. Technol.* **2007**, *190*, 138–141. [[CrossRef](#)]
35. Yilmaz, O. Effect of welding parameters on diffusion bonding of type 304 stainless steel–copper bimetal. *Mater. Sci. Technol.* **2001**, *17*, 989–994. [[CrossRef](#)]
36. Akhter, J.; Ahmad, M.; Iqbal, M.; Akhtar, M.; Shaikh, M. Formation of dendritic structure in the diffusion zone of the bonded Zircaloy-4 and stainless steel 316L in the presence of Ti interlayer. *J. Alloy. Compd.* **2005**, *399*, 96–100. [[CrossRef](#)]
37. AlHaza, A.; Haneklaus, N.; Almutairi, Z. Impulse pressure-assisted diffusion bonding (IPADB): Review and outlook. *Metals* **2021**, *11*, 323. [[CrossRef](#)]
38. Azizi, A.; Alimardan, H. Effect of welding temperature and duration on properties of 7075 Al to AZ31B Mg diffusion bonded joint. *Trans. Nonferrous Met. Soc. China* **2016**, *26*, 85–92. [[CrossRef](#)]

39. Li, P.; Wang, L.; Yan, S.; Meng, M.; Xue, K. Temperature effect on the diffusion welding process and mechanism of B2–O interface in the Ti2AlNb-based alloy: A molecular dynamics simulation. *Vacuum* **2020**, *173*, 109118. [[CrossRef](#)]
40. Akca, E.; Gursel, A. The effect of diffusion welding parameters on the mechanical properties of titanium alloy and aluminum couples. *Metals* **2017**, *7*, 22. [[CrossRef](#)]
41. Cooke, K.O.; Atieh, A.M. Current trends in dissimilar diffusion bonding of titanium alloys to stainless steels, aluminium and magnesium. *J. Manuf. Mater. Process.* **2020**, *4*, 39. [[CrossRef](#)]
42. Wang, J.; Li, Y.; Huang, W. Interface microstructure and diffusion kinetics in diffusion bonded Mg/Al joint. *React. Kinet. Catal. Lett.* **2008**, *95*, 71–79. [[CrossRef](#)]
43. Song, T.; Jiang, X.; Shao, Z.; Fang, Y.; Mo, D.; Zhu, D.; Zhu, M. Microstructure and mechanical properties of vacuum diffusion bonded joints between Ti-6Al-4V titanium alloy and AISI316L stainless steel using Cu/Nb multi-interlayer. *Vacuum* **2017**, *145*, 68–76. [[CrossRef](#)]
44. Fang, Y.; Jiang, X.; Mo, D.; Song, T.; Luo, Z. Microstructure and mechanical properties of the vacuum diffusion bonding joints of 4J29 kovar alloy and 316L stainless steel using pure cobalt interlayer. *Vacuum* **2019**, *168*, 108847. [[CrossRef](#)]
45. AlHazaa, A.; Haneklaus, N. Diffusion bonding and transient liquid phase (TLP) bonding of type 304 and 316 austenitic stainless steel—A review of similar and dissimilar material joints. *Metals* **2020**, *10*, 613. [[CrossRef](#)]
46. Islam, M.; Ridlev, N. Isostatic diffusion bonding of a microduplex stainless steel. *Scr. Mater.* **1998**, *38*, 1187–1193. [[CrossRef](#)]
47. Lee, H.-S. Diffusion bonding of metal alloys in aerospace and other applications. In *Welding and Joining of Aerospace Materials*, 2nd ed.; Chaturvedi, M., Ed.; Woodhead Publishing Series Elsevier Ltd.: Cambridge, UK, 2021.
48. Kim, S.-J.; Gil Lee, C.; Lee, T.-H.; Oh, C.-S. Effect of Cu, Cr and Ni on mechanical properties of 0.15 wt.% C TRIP-aided cold rolled steels. *Scr. Mater.* **2003**, *48*, 539–544. [[CrossRef](#)]
49. Zhang, C.; Li, H.; Li, M. Formation mechanisms of high quality diffusion bonded martensitic stainless steel joints. *Sci. Technol. Weld. Join.* **2015**, *20*, 115–122. [[CrossRef](#)]
50. Hua, Y.; Chen, J.; Yu, L.; Si, Y.; Liu, C.; Li, H.; Liu, Y. Microstructure evolution and mechanical properties of dissimilar material diffusion-bonded joint for high Cr ferrite heat resistant steel and austenitic heat resistant steel. *Acta Metall. Sin.* **2021**, *58*, 141–154.
51. Noh, S.; Kasada, R.; Kimura, A. Solid-state diffusion bonding of high-Cr ODS ferritic steel. *Acta Mater.* **2011**, *59*, 3196–3204. [[CrossRef](#)]
52. Shi, Y.; Liu, J.; Yan, Y.; Xia, Z.; Lei, Y.; Guo, F.; Li, X. Creep properties of composite solders reinforced with nano-and micro-sized particles. *J. Electron. Mater.* **2008**, *37*, 507–514. [[CrossRef](#)]
53. Hull, D.; Rimmer, D. The growth of grain-boundary voids under stress. *Philos. Mag.* **1959**, *4*, 673–687. [[CrossRef](#)]
54. Wang, D.; Xiu, S. Effect of bonding temperature on the interfacial micro-structure and performance of mild steel/austenitic stainless steel diffusion-bonded joint. *Acta Metall. Sin.* **2017**, *53*, 567–574. [[CrossRef](#)]
55. Kurt, B.; Orhan, N.; Ozel, S. Interface microstructure of diffusion bonded austenitic stainless steel and medium carbon steel couple. *Sci. Technol. Weld. Join.* **2007**, *12*, 197–201. [[CrossRef](#)]
56. Raynor, G.V.; Rivlin, V.G. *Phase Equilibria in Iron Ternary Alloys—A Critical Assessment of the Experimental Literature*; The Institute of Metals: London, UK, 1988.
57. Frost, H.J.; Ashby, M.F. *Deformation Mechanism Maps: The Plasticity and Creep of Metals and Ceramics*; Pergamon press: Elmsford, NY, USA, 1982.
58. Trapp, J.; Semenov, A.; Nöthe, M.; Wallmersperger, T.; Kieback, B. Fundamental principles of spark plasma sintering of metals: Part III—densification by plasticity and creep deformation. *Powder Metall.* **2020**, *63*, 329–337. [[CrossRef](#)]
59. Sopoušek, J.; Foret, R.; Jan, V. Simulation of dissimilar weld joints of steel P91. *Sci. Technol. Weld. Join.* **2004**, *9*, 59–64. [[CrossRef](#)]
60. Race, J.; Bhadeshia, H. Carbon migration across dissimilar steel welds. In *International Trends in Welding Science and Technology*; ASM International: Almere, The Netherlands, 1993; pp. 1–5.
61. Gomez, X.; Echeberria, J. Microstructure and mechanical properties of low alloy steel T11–austenitic stainless steel 347H bimetallic tubes. *Mater. Sci. Technol.* **2000**, *16*, 187–193. [[CrossRef](#)]
62. Silva, C.C.; Miranda, H.C.; de Sant’Ana, H.B.; Farias, J.P. Austenitic and ferritic stainless steel dissimilar weld metal evaluation for the applications as-coating in the petroleum processing equipment. *Mater. Des.* **2013**, *47*, 1–8. [[CrossRef](#)]
63. Mas, F.; Tassin, C.; Valle, N.; Robaut, F.; Charlot, F.; Yescas, M.; Roch, F.; Todeschini, P.; Bréchet, Y. Metallurgical characterization of coupled carbon diffusion and precipitation in dissimilar steel welds. *J. Mater. Sci.* **2016**, *51*, 4864–4879. [[CrossRef](#)]
64. Lippold, J.C.; Kotecki, D.J. *Welding Metallurgy and Weldability of Stainless Steels*; Wiley-Interscience: New York, NY, USA, 2005.
65. Thomas, W.M.; Nicholas, E.D.; Needham, J.C.; Murch, M.G.; Temple-Smith, P.; Dawes, C.J. *International Patent Application PCT/GB92/02203 and GB Patent Application 9125978.8*; UK Patent Office: London, UK, 1991; p. 6.
66. Wang, Y.; Tsutsumi, S.; Kawakubo, T.; Fujii, H. Microstructure and mechanical properties of weathering mild steel joined by friction stir welding. *Mater. Sci. Eng. A* **2021**, *823*, 141715. [[CrossRef](#)]
67. Ibrahim, I.R.; Khedr, M.; Mahmoud, T.S.; Abdel-Aleem, H.A.; Hamada, A. Study on the mechanical performance of dissimilar butt joints between low Ni medium-Mn and Ni-Cr austenitic stainless steels processed by gas tungsten arc welding. *Metals* **2021**, *11*, 1439. [[CrossRef](#)]
68. Suman, S.; Biswas, P. Comparative study on SAW welding induced distortion and residual stresses of CSEF steel considering solid state phase transformation and preheating. *J. Manuf. Process.* **2020**, *51*, 19–30. [[CrossRef](#)]

69. Meng, X.; Huang, Y.; Cao, J.; Shen, J.; dos Santos, J.F. Recent progress on control strategies for inherent issues in friction stir welding. *Prog. Mater. Sci.* **2021**, *115*, 100706. [[CrossRef](#)]
70. Meng, X.; Xie, Y.; Ma, X.; Liang, M.; Peng, X.; Han, S.; Kan, L.; Wang, X.; Chen, S.; Huang, Y. Towards friction stir remanufacturing of high-strength aluminum components. *Acta Metall. Sin. Engl. Lett.* **2022**, 1–12. [[CrossRef](#)]
71. Sunilkumar, D.; Muthukumaran, S.; Vasudevan, M.; Reddy, G.M. Microstructure and mechanical properties relationship of friction stir-and A-GTA-welded 9Cr-1Mo to 2.25 Cr-1Mo steel. *J. Mater. Eng. Perform.* **2021**, *30*, 1221–1233. [[CrossRef](#)]
72. Sunilkumar, D.; Muthukumaran, S.; Vasudevan, M.; Reddy, M.G. Effect of friction stir and activated-GTA welding processes on the 9Cr-1Mo steel to 316LN stainless steel dissimilar weld joints. *Sci. Technol. Weld. Join.* **2020**, *25*, 311–319. [[CrossRef](#)]
73. Abd-Elaziem, W.; Khedr, M.; Newishy, M.; Abdel-Aleem, H. Metallurgical characterization of a failed A106 Gr-B carbon steel welded condensate pipeline in a petroleum refinery. *Int. J. Press. Vessel. Pip.* **2022**, *200*, 104843. [[CrossRef](#)]
74. Wang, Z.W.; Xie, G.M.; Wang, D.; Zhang, H.; Ni, D.R.; Xue, P.; Xiao, B.L.; Ma, Z.Y. Microstructural evolution and mechanical behavior of friction-stir-welded DP1180 advanced ultrahigh strength steel. *Acta Metall. Sin. Engl. Lett.* **2020**, *33*, 58–66. [[CrossRef](#)]
75. Sekban, S.M.; Xue, P.; Ma, Z.Y.; Purcek, G. Shipbuilding. *Mater. Sci. Eng. A* **2016**, *672*, 40–48. [[CrossRef](#)]
76. Venkatakrishna, A.; Lakshminarayanan, A.; Vasantharaja, P.; Vasudevan, M. Decisive impact of Filler-free joining processes on the Microstructural evolution, tensile and impact properties of 9Cr-1Mo-V-Nb to 316 L (N) dissimilar joints. *Proc. Inst. Mech. Eng. Part C J. Mech. Eng. Sci.* **2022**, *236*, 2408–2427. [[CrossRef](#)]
77. Sunilkumar, D.; Muthukumaran, S.; Vasudevan, M.; Reddy, M. Tool rotational speed variant response on the evolution of microstructure and its significance on mechanical properties of friction stir welded 9Cr-1Mo steel. *J. Mater. Process. Technol.* **2020**, *278*, 116536.
78. Wang, H.; Wang, K.; Wang, W.; Huang, L.; Peng, P.; Yu, H. Microstructure and mechanical properties of dissimilar friction stir welded type 304 austenitic stainless steel to Q235 low carbon steel. *Mater. Charact.* **2019**, *155*, 109803. [[CrossRef](#)]
79. Rai, R.; De, A.; Bhadeshia, H.K.D.H.; Debroy, T. Review: Friction stir welding tools. *Sci. Technol. Weld. Join.* **2011**, *16*, 325–342. [[CrossRef](#)]
80. Ghosh, M.; Kumar, K.; Mishra, R. Friction stir lap welded advanced high strength steels: Microstructure and mechanical properties. *Mater. Sci. Eng. A* **2011**, *528*, 8111–8119. [[CrossRef](#)]
81. Sunilkumar, D.; Muthukumaran, S.; Vasudevan, M.; Selvi, S.P.; Reddy, M.G. Effect of tool rotation speed on microstructure and hardness of friction-stir-welded 9Cr-1Mo steel. *Trans. Indian Inst. Met.* **2019**, *72*, 1537–1540. [[CrossRef](#)]
82. Wang, X.; Gao, Y.; McDonnell, M.; Feng, Z. Determination of the friction stir welding window from the solid-state-bonding mechanics under severe thermomechanical conditions. *Materialia* **2022**, *21*, 101350. [[CrossRef](#)]
83. Wang, X.; Gao, Y.; Liu, X.; McDonnell, M.; Feng, Z. Tool-workpiece stick-slip conditions and their effects on torque and heat generation rate in the friction stir welding. *Acta Mater.* **2021**, *213*, 116969. [[CrossRef](#)]
84. Ragab, M.; Liu, H.; Yang, G.-J.; Ahmed, M. Friction stir welding of 1Cr11Ni2W2MoV martensitic stainless steel: Numerical simulation based on coupled Eulerian Lagrangian approach supported with experimental work. *Appl. Sci.* **2021**, *11*, 3049. [[CrossRef](#)]
85. Ragab, M.; Liu, H.; Ahmed, M.M.; Yang, G.-J.; Lou, Z.-J.; Mehboob, G. Microstructure evolution during friction stir welding of 1Cr11Ni2W2MoV martensitic stainless steel at different tool rotation rates. *Mater. Charact.* **2021**, *182*, 111561. [[CrossRef](#)]
86. Wang, Z.; Zhang, J.; Xie, G.; Wu, L.; Zhang, H.; Xue, P.; Ni, D.; Xiao, B.; Ma, Z. Evolution mechanisms of microstructure and mechanical properties in a friction stir welded ultrahigh-strength quenching and partitioning steel. *J. Mater. Sci. Technol.* **2022**, *102*, 213–223. [[CrossRef](#)]
87. Wang, Z.; Zhang, H.; An, X.; Wu, L.; Xue, P.; Zhang, Q.; Ni, D.; Xiao, B.; Ma, Z. Achieving equal strength joint to parent metal in a friction stir welded ultra-high strength quenching and partitioning steel. *Mater. Sci. Eng. A* **2020**, *793*, 139979. [[CrossRef](#)]
88. Trzaska, J.; Dobrzański, L. Modelling of CCT diagrams for engineering and constructional steels. *J. Mater. Process. Technol.* **2007**, *192*, 504–510. [[CrossRef](#)]
89. Johnson, P.; Murugan, N. Microstructure and mechanical properties of friction stir welded AISI321 stainless steel. *J. Mater. Res. Technol.* **2020**, *9*, 3967–3976. [[CrossRef](#)]
90. Johnson, P.; Murugan, N. Friction stir welding of 321stainless steel plates by tungsten lanthanum tool and its joint analyses. *Mater. Today Proc.* **2018**, *5*, 4235–4241. [[CrossRef](#)]
91. Kumar, S.S.; Murugan, N.; Ramachandran, K. Influence of tool material on mechanical and microstructural properties of friction stir welded 316L austenitic stainless steel butt joints. *Int. J. Refract. Met. Hard Mater.* **2016**, *58*, 196–205. [[CrossRef](#)]
92. Ramesh, R.; Dinaharan, I.; Kumar, R.; Akinlabi, E.T. Microstructure and mechanical characterization of friction-stir-welded 316L austenitic stainless steels. *J. Mater. Eng. Perform.* **2019**, *28*, 498–511. [[CrossRef](#)]
93. Shashi Kumar, S.; Murugan, N.; Ramachandran, K. Effect of friction stir welding on mechanical and microstructural properties of AISI 316L stainless steel butt joints. *Weld. World* **2019**, *63*, 137–150. [[CrossRef](#)]
94. Sekban, D.; Aktarer, S.; Purcek, G. Friction stir welding of low-carbon shipbuilding steel plates: Microstructure, mechanical properties, and corrosion behavior. *Metall. Mater. Trans. A* **2019**, *50*, 4127–4140. [[CrossRef](#)]
95. Ramesh, R.; Dinaharan, I.; Kumar, R.; Akinlabi, E. Microstructure and mechanical characterization of friction stir welded high strength low alloy steels. *Mater. Sci. Eng. A* **2017**, *687*, 39–46. [[CrossRef](#)]

96. Sauraw, A.; Sharma, A.K.; Fydrych, D.; Sirohi, S.; Gupta, A.; Świerczyńska, A.; Pandey, C.; Rogalski, G. Study on microstructural characterization, mechanical properties and residual stress of gtaw dissimilar joints of p91 and p22 steels. *Materials* **2021**, *14*, 6591. [[CrossRef](#)]
97. Rahimi, S.; Konkova, T.N.; Violatos, I.; Baker, T.N. Evolution of microstructure and crystallographic texture during dissimilar friction stir welding of duplex stainless steel to low carbon-manganese structural steel. *Metall. Mater. Trans. A* **2019**, *50*, 664–687. [[CrossRef](#)]
98. Wang, W.; Wang, Z.; Xu, L.; Hu, Y.; Zhao, H. Dissimilar friction stir welding of austenitic and duplex stainless steel: Effect of material position and tool Offset. *Steel Res. Int.* **2020**, *91*, 2000156. [[CrossRef](#)]
99. Bin Matlan, M.J.; Mohebbi, H.; Pedapati, S.R.; Awang, M.B.; Ismail, M.C.; Kakooei, S.; Dan, N.E. Dissimilar friction stir welding of carbon steel and stainless steel: Some observation on microstructural evolution and stress corrosion cracking performance. *Trans. Indian Inst. Met.* **2018**, *71*, 2553–2564. [[CrossRef](#)]
100. Tiwari, A.; Singh, P.; Pankaj, P.; Biswas, P.; Kore, S.D.; Pal, S. Effect of tool offset and rotational speed in dissimilar friction stir welding of AISI 304 stainless steel and mild steel. *J. Mater. Eng. Perform.* **2019**, *28*, 6365–6379. [[CrossRef](#)]
101. İpekoğlu, G.; Küçükömeroğlu, T.; Aktarer, S.M.; Sekban, D.M.; Çam, G. Investigation of microstructure and mechanical properties of friction stir welded dissimilar St37/St52 joints. *Mater. Res. Express* **2019**, *6*, 046537. [[CrossRef](#)]

**Disclaimer/Publisher’s Note:** The statements, opinions and data contained in all publications are solely those of the individual author(s) and contributor(s) and not of MDPI and/or the editor(s). MDPI and/or the editor(s) disclaim responsibility for any injury to people or property resulting from any ideas, methods, instructions or products referred to in the content.